Bestimmung der Ladung des Top Quarks mit dem ATLAS Experiment

Masterarbeit

zur Erlangung des akademischen Grades

Master of Science
(M.Sc.)

dem Fachbereich Physik der
Universität Siegen

vorgelegt von

Oliver Rosenthal

Dezember 2009

Contents

List of Tables

List of Figures

Chapter 1

Introduction

It is widely believed that the particle discovered at the Fermilab National Accelerator Laboratory in 1995 is the long-sought top quark, completing the three-generation structure of the Standard Model. This assumption can only be verified if the properties of this quark are completely investigated and the results are consistent with the Standard Model expectations. In particular, measurements of the D0 and the CDF collaboration have not definitely confirmed that the discovered quark has an electric charge of $\frac{2}{3}$e and hence the expected Standard Model charge of the top quark. Up to now, it has not been ruled out that the new particle is an exotic quark with a charge of $-\frac{4}{3}$e [42, 43], while the "real" top quark has not been discovered yet.

Basically, there are two methods to determine the electric charge of the top quark, an indirect measurement via the top decay products and a second technique based on the direct measurement of the top quark electromagnetic coupling through photon radiation in top pair events. The two Tevatron collaborations have only been able to perform first measurements via the top decay products due to the low statistic of $t\bar{t}\gamma$ events [42, 43], but it is expected that the Large Hadron Collider will produce a sufficent number of $t\bar{t}\gamma$ events to also perform the direct charge measurement.

This thesis focuses on the direct measurement technique via photon radiation in top quark events, and therefore studies radiative top quark processes for the two possible top quark charges. After analyses on parton and detector level, this thesis will determine the discrimination between the Standard Model top quark and the exotic top quark using pp$\rightarrow$b$\bar{\text{b}}$q$_1\bar{\text{q}}_2$e$^{\pm}\nu_e\gamma$ events detected with the ATLAS experiment at a center of mass energy of 10 TeV.

This thesis is structured as follows:

- The Standard Model of particles physics is briefly recalled in chapter 2 with the main focus given to the top quark production and decay mechanism in proton-proton collisions.

- Chapter 3 gives a brief description of the Large Hadron Collider at CERN and discusses the design and performance of the ATLAS detector.

- Chapter 4 shows the analysis results on parton level. The first sections deals with the two possible values of the top quark charge and the two measuring techniques in

detail. After the introduction of the Monte Carlo generator WHIZARD, the calculated cross sections and a variety of kinematic distributions are discussed in order to find differences between the two top quark models. In the last section, results of a previous analysis are reproduced and compared.

- The generation of samples including the response of the ATLAS detector is discussed at the beginning of chapter 5. After a detailed description of the event selection used in this analysis, the discrimination between both top quark models is determined.

- The last chapter summarizes this thesis and gives an outlook on the further prospects of the top quark charge measurement.

Chapter 2

Top Quark Physics

The discovery of the top quark at Tevatron in 1995 [1, 2] finally completed the three generation structure of the Standard Model as the isospin partner of the bottom quark. Its existence was predicted long before, as the the bottom quark was already discovered 18 years before [3], but only the proton antiproton accelerator Tevatron at Fermilab in the USA was able to achieve such high energies, to produce this by far heaviest quark with a current world average mass of [4]

$$m_t = 173.1 \pm 0.6(\text{stat.}) \pm 1.1(\text{syst.})\,\text{GeV}.$$

2.1   The Standard Model Of Particle Physics

The Standard Model [5, 6] of elementary particle physics describes the constituents of matter and the interactions between them. Basically, matter consists of only a few fundamental particles with spin 1/2, which are called fermions, while the interactions are mediated by the spin 1 bosons.

The class of fermions consists of a total of 12 particles and their respective antiparticles, which are subdivided into leptons and quarks. The leptons are the electron e^-, the muon μ^-, the tau τ^- and the corresponding neutrinos ν_e, ν_μ and ν_τ. The quarks are called up u, down d, charm c, strange s, top t and bottom b. Both types of fermions can be grouped together in three families. Each of these families consists of two leptons and two quarks: a massive lepton with the electric charge of -1e, with e being the elementary charge, and a almost massless neutrino without any electric charge, as well as a pair of quarks with an electric charge of $+\frac{2}{3}$e and $-\frac{1}{3}$e. These two quarks are generally called up-type and down-type quark with respect to the names of the first family. In one family, the two leptons and quarks each form left-handed weak isospin doublets, since the two quarks and the two leptons are identical with regard to the weak interaction. The quarks as well as the charged leptons exist also as right-handed singlets.

Ordinary atoms consist only of fermions of the first family with up and down quarks composing the nucleon and electrons filling the shell, as the other charged fermions are each much heavier than the corresponding first-family particles.

The gauge bosons are the carriers of the fundamental interactions. Four kinds of gauge bosons have been discovered: The photon is a massless and chargeless particle transmit-

ting electromagnetic interactions, the massive vector bosons W^+, W^- and Z mediate the weak force, while the eight gluons are exchanged between quarks in the strong interaction. All Standard Model particles are illustrated in Figure 2.1, listing their mass, electric charge and spin values.

Figure 2.1: Illustration of the Standard Model of particle physics [7].

2.2   The Higgs Mechanism

The existence of massive gauge bosons in weak interactions is explained in the Standard Model by the Higgs mechanism [8]. This mechanism postulates an additional symmetry breaking background field with its field quantum, the Higgs boson H, coupling to the W and Z bosons causing an effective mass. Assuming Yukawa couplings the Higgs mechanism could also explain the fermion masses. As the Higgs boson has not been observed yet in any experiment, it must obtain a high mass from its self-coupling. Experiments so far exclude a Higgs boson mass below $114.4\,\text{GeV}$ [9] and theoretical assumptions limit the mass window to $1\,\text{TeV}$ at the most.

2.3   Fundamental Interactions

All physics phenomena are based on four fundamental interactions, of which three are included in the Standard Model [5, 6]. The interactions have specific properties, as not every elementary particle is subject to every force. In a process, the particles have to carry the corresponding charge that couples to the specific force, while the gauge bosons are exchanged between them as mediators.
The interactions are described by quantum field theories (QFT) [10] providing very precise predictions. All QFTs have to agree to various conditions: The Lorentz invariance, the local gauge invariance and the renormalization. The Lorentz invariance requires that each

theory must hold in every reference frame. The local gauge invariance indicates that a physical field is unchanged under every gauge transformation, while the renormalization corrects the original Lagrangian of a quantum field theory to eliminate any divergencies. The fundamental interactions are described in the QFTs by quantized fields, while the mediating gauge bosons are the quanta of the field.

2.3.1   Strong Interaction

The quantum chromodynamics (QCD) is the quantum field theory of the strong interaction, with the quarks and gluons as the only subjects to this force and the gluons as the mediators. There are three kinds of charge called color which are carried by quarks: red (r), green (g), blue (b) and their respective 'anti'-charges. Since gluons are exchanged between two different colored quarks, they always carry combinations of color. As the Dirac's equation has to be invariant under the local SU(3) color transformation according to the QCD, there are eight possible color combinations resulting in eight different gluons:

$$r\bar{g}, r\bar{b}, b\bar{r}, b\bar{g}, g\bar{b}, g\bar{r}, \sqrt{\frac{1}{2}}(r\bar{r} - g\bar{g}), \sqrt{\frac{1}{6}}(r\bar{r} - g\bar{g} - 2b\bar{b}).$$

Although a gluon is massless with no electrical charge, the strong interaction does not have an infinite range as the gluons interact with each other due to their color charges. Due to the self-coupling of the gluons the effective coupling α_s of QCD approaches zero with increasing energy. At high energies, the coupling can be described in a first order calculation by

$$\alpha_s(Q^2) = \frac{12\pi}{(33 - 2n_f)\ln(\frac{Q^2}{\Lambda_{QCD}^2})}$$

where $Q^2=-q^2$ is the momentum transfered by the gluons in an interaction and n_f the number of flavors. The parameter Λ_{QCD} is called the energy scale of the strong interaction, because the coupling is strong enough around $Q^2=\Lambda_{QCD}^2$ to arrange the quarks into bound states called hadrons. These hadrons are color-neutral particles occuring in two different types: Mesons, which comprise a pair of quark and antiquark, and hadrons, which are composed of three quarks, e.g. the proton (uud). At large energies $Q^2 > \Lambda_{QCD}^2$ the coupling is small and the quarks are less bound by the strong force, known as asymptotic freedom. The world average of the coupling α_s, which has been measured in various experiments at different energy scales, has a value at an energy equal to the Z boson mass of [9]

$$\alpha_s(m_Z) = 0.1176 \pm 0.002.$$

2.3.2   Electromagnetic Interaction

The electromagnetic interaction is described by the quantum electrodynamic (QED). This theory, which symmetry group is U(1), includes every elementary particle that has non-zero electric charge, while the massless and uncharged photon γ serves as mediator with an infinite range. The coupling constant α_{QED}, which is also called the fine structure

constant, can be calculated at high Q^2 by

$$\alpha_{QED}(Q^2) = \frac{\alpha(\mu^2)}{1 - \frac{\alpha(\mu^2)}{3\pi}\ln(\frac{Q^2}{\mu^2})}$$

where $\alpha(\mu^2)$ is the reference value at a low energy renormalization momentum μ^2.

2.3.3 Weak Interaction

The weak force affects all fermions, i.e leptons and quarks. The quantum number corresponding to this interaction is called flavor, which is basically the name of the particular fermion, resulting in a total of 12 flavors. Each fermion represents an eigenstate of the weak interaction Hamiltonian. The mass eigenstates are created by the superposition of the flavor eigenstates, implying that particles can change their flavor, but leptons can only convert into leptons and quarks into quarks. The mediators of the weak interaction are the two massive bosons W^+ and W^- with masses of $m_W = (80.40\pm0.03)\,\text{GeV}$ [9] and the neutral Z^0 boson with a mass of $m_Z = (91.188\pm0.002)\,\text{GeV}$ [9]. For the quarks, the mixing probabilities are described by the Cabibbo-Kobayashi-Maskawa (CKM) matrix. Each matrix element squared $|V_{qq'}|^2$ is directly proportional to the probability of a quark q becoming a quark q' after emitting a W boson. Their values are not predicted by theory, but are obtained by measurements. The matrix with the absolute values of its elements is given by [9]

$$|V_{CKM}| = \begin{pmatrix} |V_{ud}| & |V_{us}| & |V_{ub}| \\ |V_{cd}| & |V_{cs}| & |V_{cb}| \\ |V_{td}| & |V_{ts}| & |V_{tb}| \end{pmatrix} = \begin{pmatrix} 0.9738 & 0.2272 & 0.0040 \\ 0.2271 & 0.9730 & 0.0422 \\ 0.0081 & 0.0416 & 0.9991 \end{pmatrix}.$$

2.4 Hadronization

As mentioned before, quarks are not observable as free particles, but appear in bound states, i.e. hadrons. During the transformation of single quarks from the scattering process into final hadrons, $q\bar{q}$ pairs are created from the gluon field between the original quarks until all quarks are bound into mesons or baryons. Thus, a high-energy quark produces a bundle of hadrons, forming a so-called particle jet (Figure 2.2). The mechanism is called hadronization, causing jets from quarks, but in a analog way also from gluons.

2.5 Hadron Collisions

At hadron colliders like the LHC, particles are produced from the interactions between the proton constituents, i.e. partons. A proton consists not only of the three valence quarks, but also of quarks and anti-quarks by vacuum fluctuations, i.e sea quarks, and gluons from the interconnecting color field. Therefore, collisions of two hadrons are initially hard
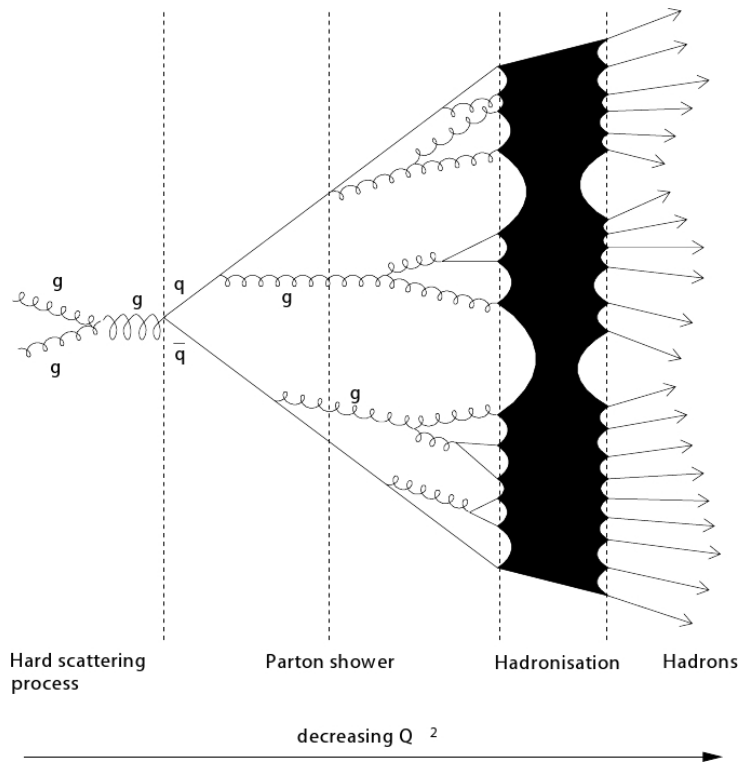
Figure 2.2: Illustration of the hadronization process [11].

scattering processes of quarks and gluons, each carrying a momentum fraction x of the parent proton. The structure function of the proton is described by

$$F(x, Q^2) = \sum_i e_i^2 x f_i(x, Q^2).$$

The summation runs over each parton i with its electric charge e_i and $f_i(x_i, Q^2)$ representing the probability of the parton to carry the momentum fraction x at the energy scale Q^2. These parton density functions $f_i(x_i, Q^2)$ cannot be calculated because of non-perburbative QCD involved, but are extracted by global QCD fits from deep inelastic scattering experiments (Figure 2.3).

The total cross section for a 2→2 reaction in a proton-proton scattering process is calculated by the sum over all allowed parton combinations of the individual cross sections folded with the proton particle density functions:

$$\sigma_{tot} = \sum_{ab} \int \int dx_a dx_b f_a(x_a, Q^2) f_b(x_b, Q^2) \sigma_{ab \to 12}.$$

2.6 Top Quark Production

At hadron colliders, top quarks are preferentially produced in $t\bar{t}$ pairs either via gluon fusion or quark anti-quark annihilation (Figure 2.4). While at the Tevatron, which is a
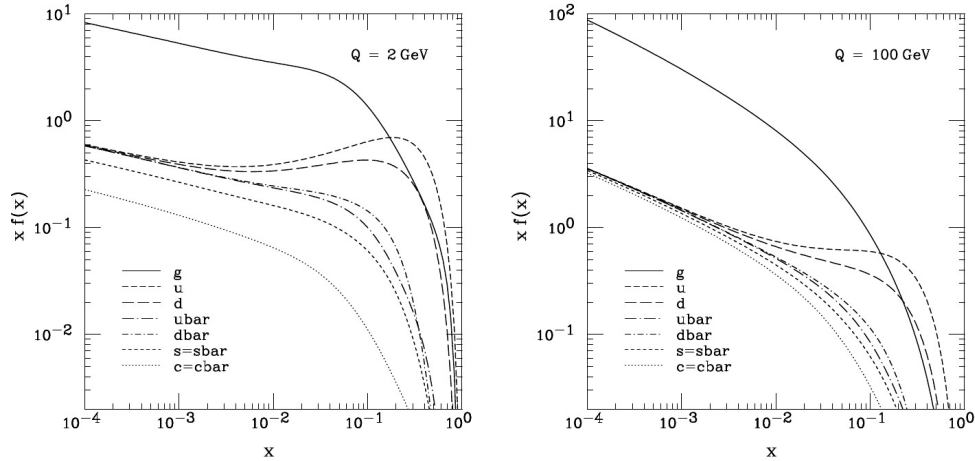
Figure 2.3: Parton distributions functions (CTEQ6M) for different partons at $Q = 2\,\text{GeV}$ (left) and $100\,\text{GeV}$ (right) [12].
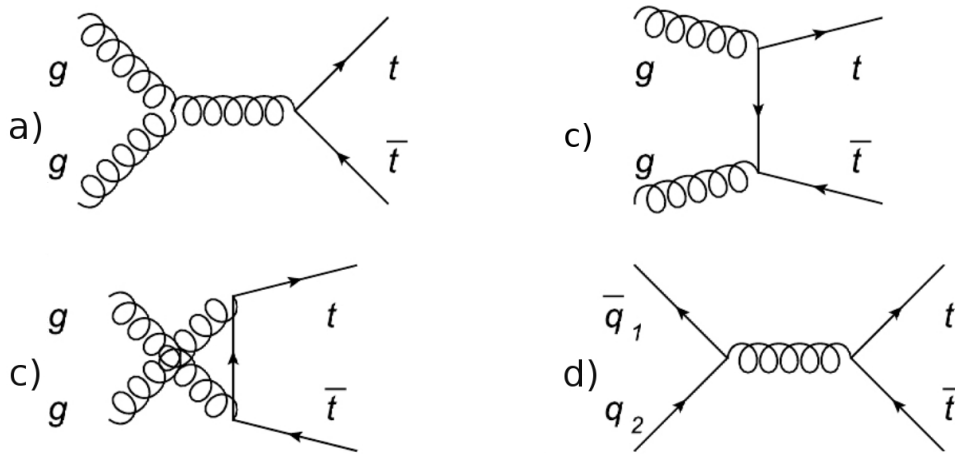
Figure 2.4: Feynman diagrams of top quark pair productions. Diagrams a) - c) represent the gluon fusion processes and diagram d) the $q\bar{q}$ annihilation process.

$p\bar{p}$-collider, the production is dominated by annihilation. At the LHC gluon fusion is preferred, because antiquarks only appear as sea quarks and gluons carry much more momentum at the much higher collision energy (LHC:up to $\sqrt{s} = 14\,\text{TeV}$, Tevatron:$\sqrt{s} = 1.96\,\text{TeV}$) due to the particle density functions. It is expected that about 87% of the top quark pairs will be produced from gluon fusion at the LHC.

The cross section of the top quark pair production can be calculated by

$$\sigma_{t\bar{t}}(\sqrt{s}, m_t, Q^2) = \sum_{ab} \int dx_a dx_b f_a(x_a, Q^2) f_b(x_b, Q^2) \times \sigma_{ab \to t\bar{t}}(\rho, m_t^2, x_a, x_b, Q^2).$$

The summation indices a,b run over all possible parton combinations ($q\bar{q}$, gg). The variable $\rho = \dfrac{4m_t^2}{\sqrt{\hat{s}}}$ depends on the effective center of mass energy $\hat{s} = x_a x_b s$ with the center of mass energy s and $x_{a,b}$ the momentum fraction of the a-th and b-th parton. The overall

Figure 2.5: Branching ratios of $t\bar{t}$ decay modes [14].

production cross section at near-next-to-next-to-leading-order (NNLO) precision is predicted to yield [13]

$$\sigma_{t\bar{t}} \approx 400\,\text{pb}$$

at a center of mass energy of $\sqrt{s} = 10\,\text{TeV}$ at the LHC.

Aside of $t\bar{t}$ pairs, also single top quarks can be produced in hadron collisions. There are three possible production mechanisms:

- The assoziated production of a top quark and a W boson

- t-channel production

- s-channel production

Single top quarks are only produced via weak interactions with a predicted total cross section of [13]

$$\sigma_t \approx 160\,\text{pb},$$

which is notizable smaller than the one for top quark pairs.

2.7 Top Quark Decay

Due to its high mass the top quark has a very short lifetime of [15]

$$\tau_{\text{top}} \approx 10^{-24}\,\text{s}$$

As the hadronic scale is about $\tau_{\text{had}} \approx 10^{-23}\,\text{s}$, the top quark is not able to build hadronic bound states, but decays via the weak interaction. According to the CKM matrix, the top quark decays almost exclusively into a bottom quark and a W boson. While the bottom quark hadronizes, the W boson decays either hadronically into a quark antiquark pair or

leptonically into a charged lepton and its corresponding neutrino. By kinematic reasons it is not possible for the W boson to decay into a top and a anti-bottom, but only into the first two quark families.

In total, there are five decay modes, three leptonic and two hadronic modes, of which the hadronic decays appear in threefold multiplicity due to the three color changes. This creates probabilities of $\frac{1}{3}$ for the leptonic and $\frac{2}{3}$ for the hadronic mode (Figure 2.5).

The are four possibilities to characterize the decay of a top quark pair by the decay of the respective W bosons [16]:

- fully hadronic $t\bar{t}$: Both W bosons decay into $q\bar{q}$ pairs resulting in a six jet final state. This decay channel is the most frequent one with a probability of 44.4%, but the most difficult to observe due to the high QCD background at the LHC.

- Semileptonic $t\bar{t}$: One W decays hadronically and the other leptonically. Because of its complex decay modes, the τ lepton is considered seperately. Due to its high branching ratio of 29.6% and a low background signature, the semileptonic channel is prefered for experimental investigations. The reason for the low background signature is the presence of high-p_T leptons, which can be used as a trigger, and large missing E_T, which can be used to separate the signal from low-Q^2 QCD background.

- Dileptonic $t\bar{t}$: Both W bosons decay into an electron or a muon plus its corresponding neutrino. Despite having two leptons and only two jets from the bottom quark, the big disadvantage of this channel is the very low probability of 4.9%

- τ-decay: Due to its high mass of m_τ=1.777 GeV it can either decay into another lepton and two neutrino or quarks and a τ neutrino, which makes the τ identification very difficult.

Exemplary Feynman diagrams of the top quark pair decays excluding the τ-leptons are shown in Figure 2.6.
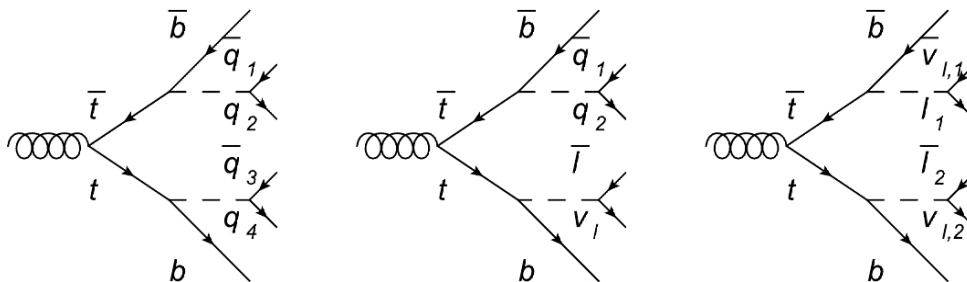
Figure 2.6: Feynman diagrams of top quark pair decay.

Chapter 3

The ATLAS Experiment

In November 2009, the high-performance particle accelerator has finally started operation, The Large Hadron Collider (LHC). It is a proton-proton collider at the European Organisation for Nuclear Research CERN on the border between France and Switzerland,near Geneva, providing a huge physics potential. Reaching much higher collision energies than any experiment before with a center of mass energy up to $\sqrt{s} = 14\,\text{TeV}$, it will offer opportunities for the search for new physics and more precise measurements of Standard Model parameters.

In September 2008, the proton beams were successfully circulated, but operations were halted due to a serious incident, where a faulty electrical connection between two bending magnets caused mechanical damage and the release of large amounts of Helium into the tunnel [17]. After the repair, proton beams were successfully circulated again on 20 November 2009 [18]. On 23 November, first collisions were recorded at the injection energy of 450 GeV per beam [19]. First high-energy collisions are expected in the first quarter of 2010 at a center of mass energy of $\sqrt{s} = 7\,\text{TeV}$, which is scheduled to be taken towards $\sqrt{s} = 10\,\text{TeV}$ in the course of 2010 [20].

3.1   The Large Hadron Collider

The LHC [21] is built at a depth between 50 and 175 m inside a 26.7 km long ring tunnel, using the infrastructure of its predecessors LEP1 and LEP2, e^+e^--colliders which operated from 1989 to 2000.

After their production, protons are bunched and accelerated in different steps [22] (Figure 3.1): First, the protons are brought up to a kinetic energy of 50 MeV in the LINAC (LINear particle ACcelerator), and then accelerated up to 1.4 GeV in the Proton Synchrotron Booster (PSB) and to 26 GeV in the Proton Synchrotron (PS). In the last step of pre-acceleration, the Super Proton Synchrotron (SPS) fills the two LHC beam pipes with 450 GeV protons. In the LHC ring, two cavity modules per beam, with a super-conducting radio-frequency of 400.8 MHz, ensure the final collision energy. Superconducting dipole magnets with a field of up to 8.3 T store the protons in the two rings. When reaching its nominal operation mode, the LHC will collide protons with an energy of 7 TeV per beam and a instantaneous luminosity of $10^{34}\text{cm}^{-2}\text{s}^{-1}$. A total of 2835 bunches, each consisting of 10^{11} protons, with a 25ns bunch spacing will collide at one of the four interaction
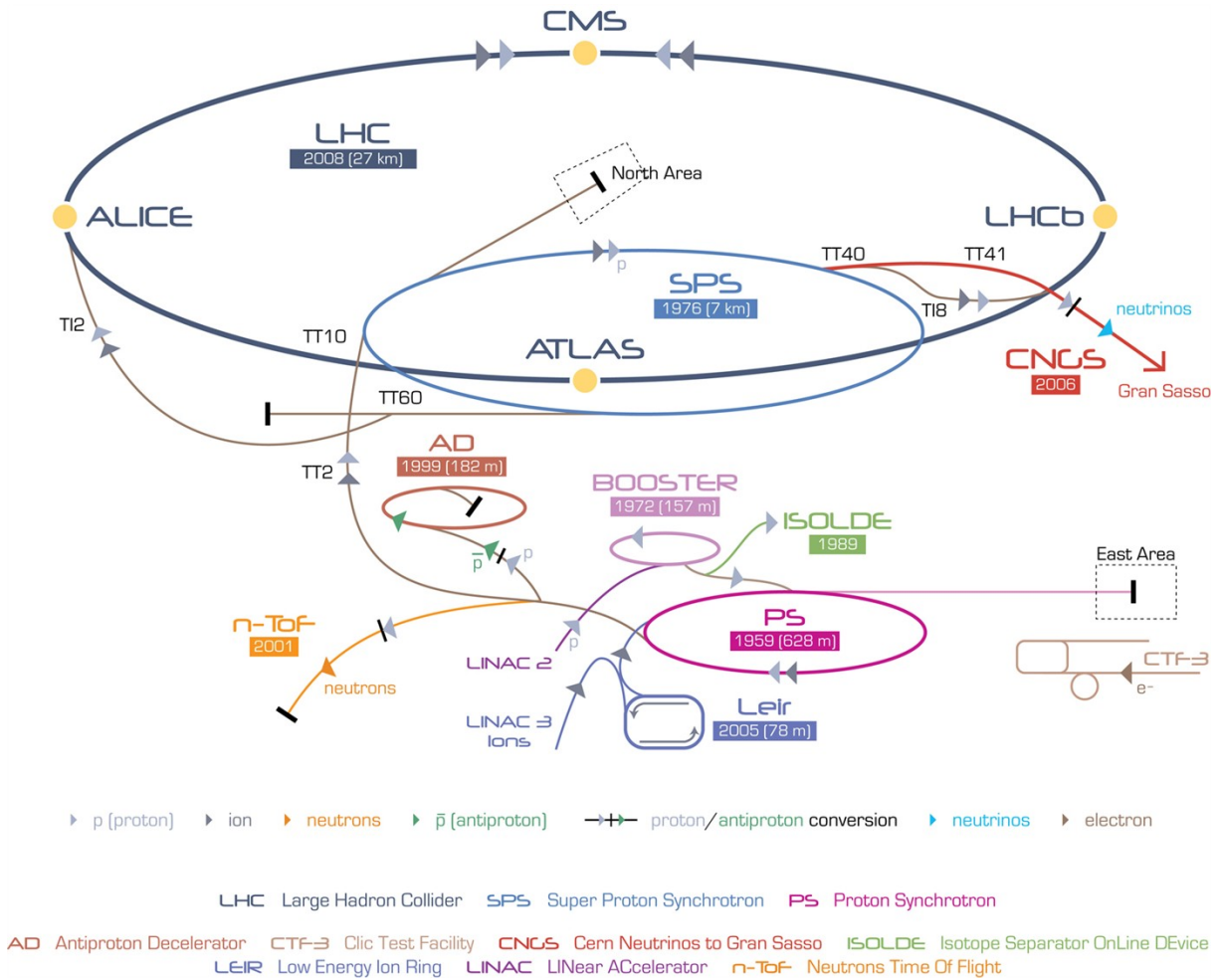
Figure 3.1: Schematic view of the CERN accelerator [26].

points, where the four detectors are located: ATLAS, CMS, LHCb and ALICE (Figure 3.2). ATLAS (A Toroidal LHC AparatuS) [28] and CMS (Compact Muon Solenoid) [23] are general purpose detectors, designed to cover a broad of Standard Model and new physics measurements. The other two experiments focus on specialized physics tasks: LHCb [24] concentrates on b-hadrons in order to investigate CP violation, while ALICE [25] is designed for the investigation of heavy ion collisions taking place in the future of the LHC.

3.2 ATLAS Detector Layout

The ATLAS detector [28] is located at injection point one of the LHC at a depth of around 80 m. It has an overall length of 44 m and 25 m in diameter with a weight of approximately 7000 t. The detector is built symmetrically around the LHC beam line with the particle interaction point in its center. Radially from the inside to the outside, ATLAS consists of an inner tracking detector, embedded into a solenoid magnet, a system of electromagnetic and hadronic calorimeters, and finally a muon system inside a large toroidal air magnet
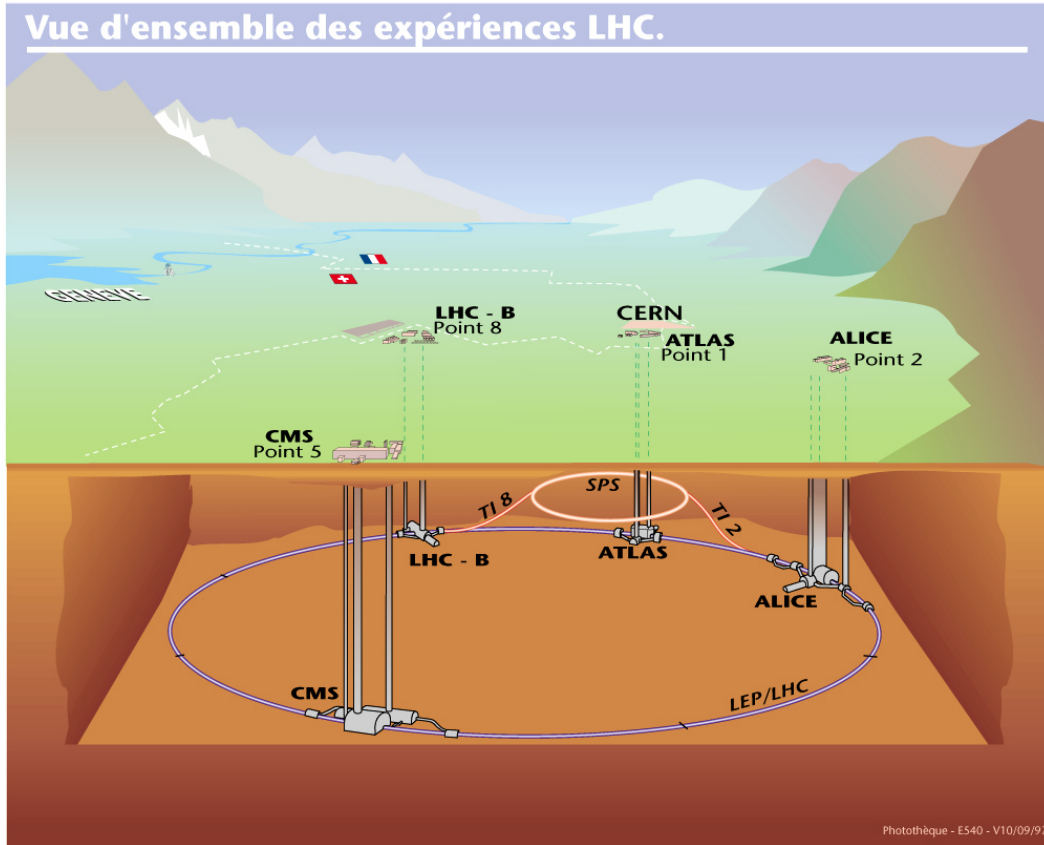
Figure 3.2: Overall view of the LHC and the locations of the four experiments [27].

(Figure 3.3).

3.3 ATLAS Coordinate System

In order to define the geometry, location and orientation of the ATLAS detector, as well as any point within it, a special coordinate system is used [28].
The interaction point in the center of the detector is defined as origin of the coordinate system, while the positive x-axis is oriented from the interaction point to the center of the LHC ring and the positive y-axis points upwards to the surface. The z-axis, which is oriented parallel to the beamline, defines the two sides of the ATLAS detector: Side A for positive values of z, pointing to the LHCb detector, and side C for negative values.
Many observables are defined in the x-y plane as they are then invariant under boosts in beam direction: The transverse momentum p_T, the transverse energy E_T and the missing transverse energy $E_{T,miss}$. The azimuthal angle ϕ is measured around the beam axis with $\phi=0$ pointing in positive x-axis, while the polar angle θ is the angle measured from the z-axis. As θ is not Lorentz invariant, it is common to use the small mass limit of the
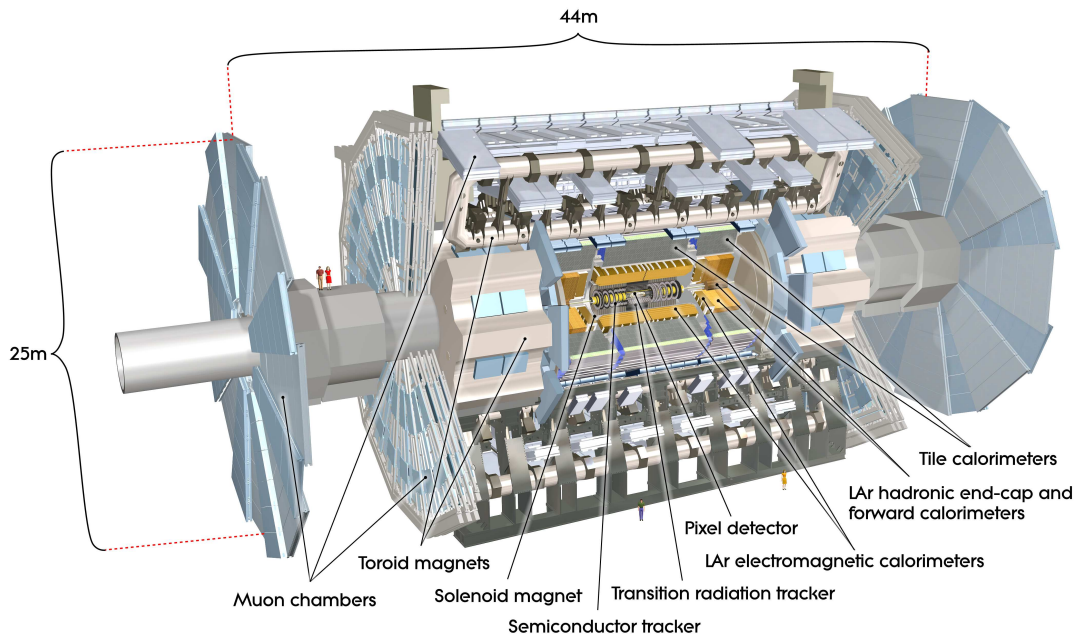
Figure 3.3: Overall layout of the ATLAS detector [28].

rapdity, the so called pseudorapidity

$$\eta = -\ln \tan\left(\frac{\theta}{2}\right).$$

Distances in the $\eta - \phi$ space are measured in

$$\Delta R = \sqrt{\Delta\eta^2 + \Delta\phi^2}.$$

3.4   The Magnet System

The magnetic field inside the ATLAS detector is provided by an solenoid and a system of three toroids [29].
The solonoid, which is aligned on the beam axis, originates a homogeneous $2\,\mathrm{T}$ axial magnetic field for the inner detector at an operating temperature of $4.5\,\mathrm{K}$. In order to not compromise the desired calorimeter performance, the superconducting solenoid magnet shares a vacuum vessel with the barrel electromagnetic calorimeter, while the iron absorber of the hadronic tile calorimeter serves as its return yoke.
A system of three air-core toroids provides the bending field for the muon spectrometer. Each toroid consists of eight superconducting coils in separate cryostats for the eight barrel coils and in a general cryostat for each of the end-caps. The magnetic field is highly non-uniform with its values varying between $0.2\,\mathrm{T}$ and $2.5\,\mathrm{T}$ for the barrel toroid an up to $3.5\,\mathrm{T}$ for the toroids at the end-caps.

3.5   The Inner Detector

The different parts of the inner detector (ID) [30, 31], the two precision tracking detectors, the pixel and the silicon microstrip tracker (SCT), as well as the straw tubes of the Transition Radiation Tracker (TRT), offer a fine detector granularity to achive an excellent momentum and vertex resolution in a range of $|\eta| < 2.5$. Within $|\eta| < 2.0$, also electron identification is provided.

With approximately 80.4 million readout channels, the pixel detector [31, 32] provides the highest granuality of the subdetectors in the ID. 1744 segmented semiconductor modules of $2\,cm \times 6.3\,cm$ size are arranged in three layers around the beampipe and on three end-cap disks on each side. Each module consist of pixels with a minimum size in R-$\phi \times$z of $50 \times 400\,\mu m^2$. The intrinsic accuracies are $10\,\mu m$ in the R-ϕ direction and $115\,\mu m$ in the second direction, which is the z-axis in the barrel and R in the disks. These properties are necessary for precise vertex measurements which are fundamental for heavy flavour and minimum bias tagging, as well as τ-identification. To minimize multiple scattering of the crossing particles, the support structure is mostly made of carbon, which has a low mass, but also a good mechanical and thermal stability.

Like the pixel detector, the SCT [31, 33] consists of semiconductor sensor modules, but has a larger granuality containing 6.3 million readout channels. In the barrel region, small-angle (40 mrad) stereo strips are installed to enable the measurement of the z-coordinate, and one set of strips in each layer is arranged parallel to the beam axis to measure the R-ϕ position. These strips consist of two 6.4 cm long daisy-chained sensors with a strip pitch of $80\,\mu m$. In the end-cap regions, the detectors have a set of radially arraged strips and a set of stereo strips at an angle of 40 mrad. The intrinsic accuracy is $17\,\mu m$ in the R-ϕ direction and $580\,\mu m$ in z direction in the barrel. The four precision space points, which are measured by the SCT, are the basis for track reconstruction.

The 4 mm diameter straw tubes of the TRT [31, 34] are able to follow tracks up to an pseudorapdity $|\eta| = 2.0$. 144 cm long straw tubes are arranged parallel to the z-axis in the barrel region, while in the end-cap region, straws with a length of 37 cm are placed radially in wheels. They are filled with a gas mixture of Xe, CO_2 and O_2 and are read out with an anode of gold plated tungsten. Each tube layer is interlaced with polypropylene fibres in the barrel and foils in the end-caps, used as transition radiation material to identify electrons. The TRT, with a total of 351,000 readout channels, only provides R-ϕ information with an intrinsic accuracy of $130\,\mu m$ per tube, but contributes significantly to the momentum measurement due to the higher number of track points and longer track length than the silicon detectors.

A cut-away view of the inner detector is shown in Figure 3.4.

3.6   The Calorimeter System

The electromagnetic (EM) and hadronic calorimeters [35, 36, 37] have to be suited for wide range of physics processes up to an pseudorapidity of $|\eta| = 4.9$. In this η-region, which is also covered by the inner detector, the EM calorimeter has a fine granularity for precision measurements of electrons, positrons and photons. The other parts of the
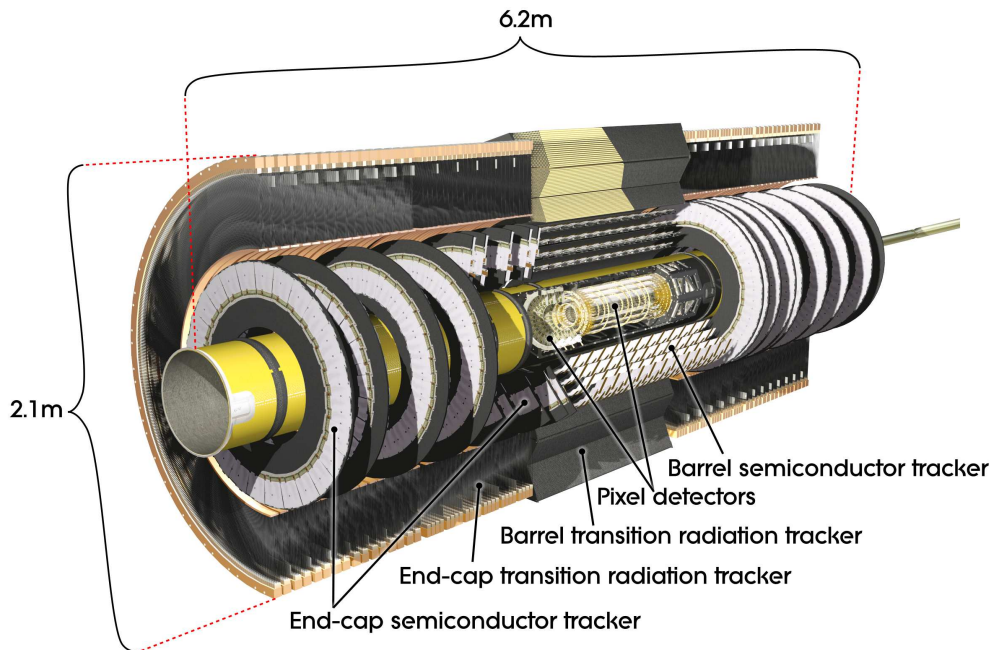
Figure 3.4: Cut-away view of the ATLAS inner detector [28].

calorimeter are devoted to jet reconstruction and $E_{T,miss}$ measurements. In addition, the calorimeter system is designed to provide input for the Level-1 trigger. Figure 3.5 shows a cut-away view of the calorimeter system.

The EM calorimeter is built using the sampling technique, utilizing liquid Argon (LAr) as the active detector medium and lead plates as the passive absorber material. The lead plates and the kapton electrodes are built in accordion geometry providing a complete ϕ symmetry without azimuthal cracks. The calorimeter consists of a barrel part up to $|\eta| = 1.475$ and an end-cap part on each side in a range of $1.375 < |\eta| < 3.2$. The barrel calorimeter is devided into two identical halves separated by a 4mm small gap at z=0, while each of the end-cap calorimeters is divided into two coaxial wheels covering the ranges $1.375 < |\eta| < 2.5$ and $2.5 < |\eta| < 3.2$. For $|\eta| < 2.5$, the EM calorimeter is segmented in three sections of depth, and for $|\eta| > 2.5$, the end-cap wheel is split in two sections in depth with a coarser granularity than the rest. For $|\eta| < 1.8$, a presampler corrects the energy lost by the electrons and photons upstream of the calorimeter.

The hadronic calorimeter consists basically of three different ones, a tile, an end-cap and a forward calorimeter.

The tile calorimeter is placed directly outside the EM calorimeter shell with its barrel covering the region up to $|\eta| = 1.0$, and two extended barrels in a range $0.8 < |\eta| < 1.7$. It is a sampling calorimeter with scintillating tiles as the active material and steel as the absorber. The tile calorimeter is radially segmented in three layers extending from an inner radius of $2.28\,\text{m}$ to an outer radius of $4.25\,\text{m}$. Two sides of the scintillating tiles are read out by wavelength shifting fibres into two seperate photomultiplier tubes, and in η, the readout cells are built by grouping fibres into the photomultipliers which are pseudo-projective towards the interaction region.
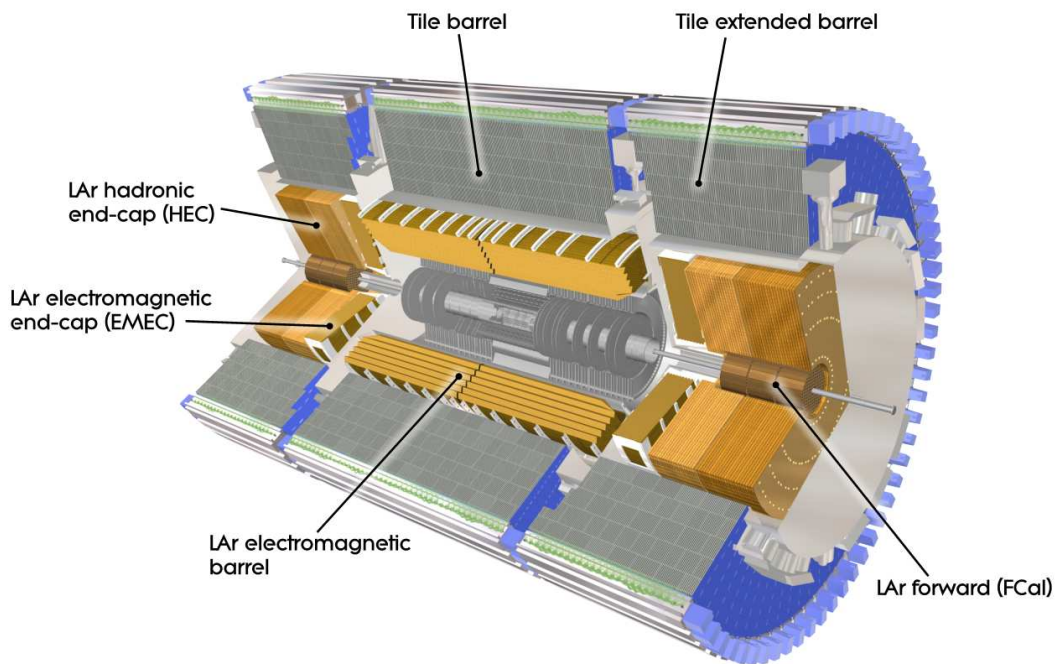
Figure 3.5: Cut-away view of the ATLAS calorimeter system [28].

The hadronic end-cap calorimeter (HEC) consists of four wheels. Two per end-cap, directly behind the end-cap electromagnetic calorimeter sharing the same liquid argon cryostats. The HEC overlaps with the forward calorimeter in the range of $3.1 < |\eta| < 3.2$ and also slightly with the tile calorimeter for $1.5 < |\eta| < 1.7$ to reduce the drop in material density. Each of the four wheels consists of 32 wedge-shaped modules, assembled with fixtures at the periphery and at the central bore, and is divided into two segments in depth. The wheels are built from parallel copper plates with $8.5 \, \text{mm}$ LAr gaps, providing the active medium for the sampling calorimeter.

In the calorimeter region near the beam pipe ($3.1 < |\eta| < 4.9$) the Forward Calorimeter (FCal) is installed. Due to its limits in depth, the FCal has a high-density design. It consists of three modules in each end-cap: The copper module is designed for electromagnetic measurements, the other two are made of tungsten and measure predominantly the energy of hadronic interactions. Each module consists of a metal matrix with regulary spaced longitudinal channels filled with concentric rods and tubes parallel to the beam line. The gaps between the rod and the tube are filled with liquid argon used as the sensitive medium. Like in the EM and the end-cap claorimeter, LAr was chosen due to its good linearity in a wide energy range, its radiation hardness and its long term stability. The signal is generated by the incoming particles ionising the argon, which means creating electron-ion pairs. These electrons drift in an electric field towards a readout electrode, where the induced current is measured.
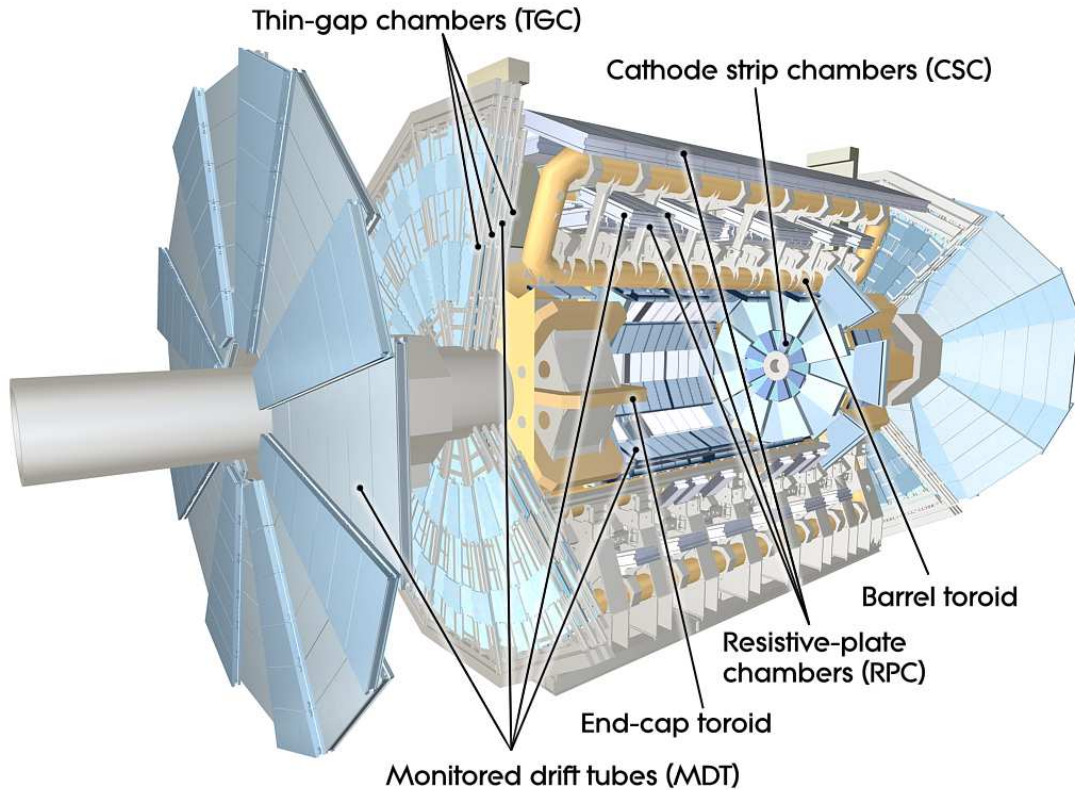
Figure 3.6: Muon system of the ATLAS detector [28].

3.7 The Muon System

The muon system [38] provides excellent muon momentum measurement in a range of $|\eta| < 2.7$ and a muon trigger signal up to $|\eta| < 2.4$. The toroidal magnet system generates a bending field which is mostly orthogonal to the muon trajectories. The muon spectrometer consists of two types of precision tracking chambers and two types of trigger chambers with a timing resolution in the order of a few nanoseconds. In the barrel region, the chambers are arranged in three cylindrical layers around the beam pipe. In the region of the end-caps they are placed in three layers perpendicular to the beam.

The monitored drift tube chambers consist of two multilayers of three or four tubes with a total of 354,000 tubes installed on 1,150 chambers. The drift tubes are made out of aluminium and filled with a gas mixture of 93% argon and 7% CO_2 at a pressure of about three bar, while tungsten-rhenium alloy wires are used as anodes.

The cathode strip chambers are multi-wire proportional chambers with strip-segmented cathodes and a higher granularity than in the other parts of the muon system to cope with the high rates in the innermost layer of the very forward region.

The resistive plate chambers consists of two parallel electrode plates at a 2 mm distance and filled with a gas mixture of $C_2H_2F_4$/Iso-C_4H_{10}/SF_6. These trigger chambers are read out by metallic strips on the outer faces via capacitive coupling.

The thin gap chambers are multi-wire proportional chambers. They are called thin gap,

because the wire-to-cathode distance of 1.4 mm is smaller than the wire-to-wire distance of 1.8mm. Used as as trigger chambers in the forward region $1.5 < |\eta| < 2.4$, these chambers have to deal with high muon rate, and therefore combine a high granularity with a highly quenching gas mixture of CO_2 and n-C_5H_{12}.

A total of 606 resistive plate chambers and 3,588 thin gap chambers perform the bunch-crossing identification, a fast muon trigger signal and measure track coordinates orthogonal to the coordinates provided by the monitored drift tube and cathode strip chambers.

3.8 The ATLAS Trigger System

In order to filter events which are considered by data analysis, a trigger system has been installed reducing the collision rate of 40 MHz to data-taking rate of 100 Hz. The trigger decision is based on three steps [39, 40], a level-1 trigger, a level-2 trigger and the event filter.

The level-1 trigger is a hardware based trigger using the information from the entire calorimeter system with reduced granularity and data from the muon system trigger chambers. It reduces the rate to about 75 kHz by selecting events which contain leptons or jets with high p_T, as well as events with large E_T or $E_{T,miss}$. These selected events define Regions-of-Interest, which are η-ϕ coordinates of detector regions where the interesting features triggering the selection have been found.

The level-2 trigger uses all available detector information within the Regions-of-Interest at full granularity and precision. This trigger reduces the rate to around 3.5 kHz.

The event filter uses offline analysis procedures to reduce the final rate down to 100 Hz. Each event has a size of approximately 1.3 MB, so that several hundreds of MB per second are written to permanent storage. A schematical overview of the trigger system is shown in Figure 3.7.

Interaction rate
~1 GHz

Bunch crossing
rate 40 MHz

LEVEL 1
TRIGGER

< 75 (100) kHz

Regions of Interest

LEVEL 2
TRIGGER

~ 1 kHz

EVENT FILTER

~ 100 Hz

CALO   MUON   TRACKING

Pipeline
memories

Derandomizers

Readout drivers
(RODs)

Readout buffers
(ROBs)

Event builder

Full-event buffers
and
processor sub-farms

Data recording
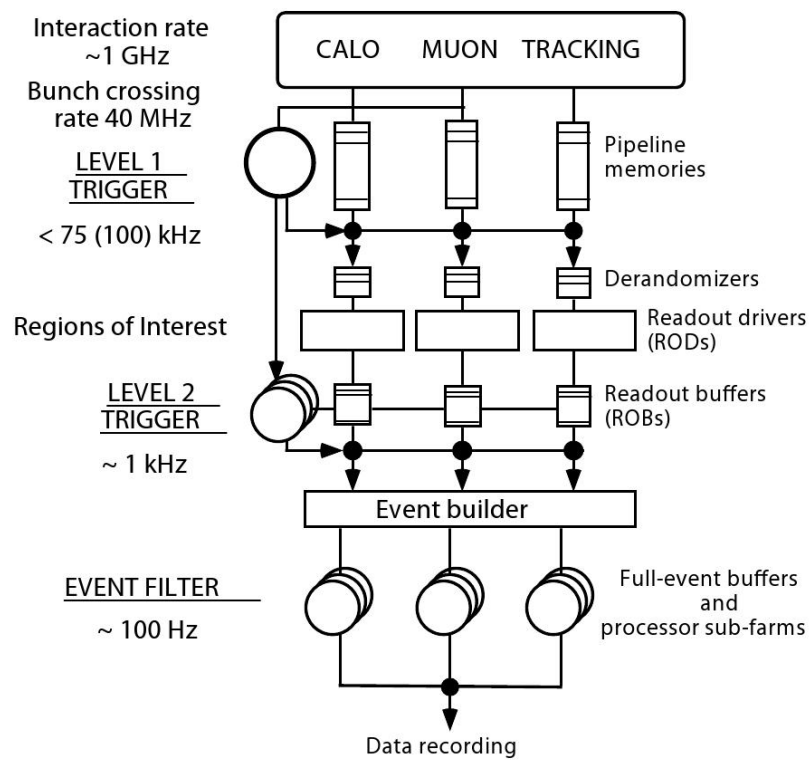
Figure 3.7: Schematical representation of the ATLAS trigger system [41].

Chapter 4

Radiative Top Quark Processes

The aim of this thesis is the determination of the electric charge of the top quark. Section 4.1 show that only two values are possible, $\frac{2}{3}$e, which is predicted by the Standard Model, or an exotic electric charge of $-\frac{4}{3}$e. Hence, the electric charge of the top quark will be determined in this analysis by finding a method to distinguish between these two possible values. Section 4.2 introduces two techniques to measure the electric charge of the top quark, of which one technique, the determination by detecting photon radiative processes, is investigated further. The Monte Carlo generator WHIZARD (Section 4.3) is used in this analysis to calculate the cross sections and generate events of radiative top quark processes for both possible top quark models. The resulting cross sections and various kinematic distributions are presented in Section 4.4 in order to compare and find differences between the Standard Model and the exotic model.

4.1 Top Quark Electric Charge

Since the discovery of the sixth quark was published in 1995, properties of the top quark like its electric charge Q_t are still poorly investigated. Although there is a strong belief that the particle discovered by the D0 and the CDF collaboration is really the up-type partner of the b-quark in the Standard Model, it is possible to interpret the discovered particle as an exotic quark with an electric charge of $-\frac{4}{3}$e. Up to now, the published top quark analyses of the two Tevatron collaborations [42, 43] include a two-fold ambiguity in pairing the bottom quarks and the W bosons in order to reconstruct the top quark. Therefore, not only the reaction t→W$^+$b, but also t* →W$^-$b is conceivable, in which case t* would be the exotic top quark.

The existence of the exotic quark can also be explained theoretically [44], as there is a possibility that the discovered particle is part of a doublet $(Q_1,Q_4)_R$. In this doublet, Q_1 has an electric charge of $-\frac{1}{3}$e and mixes with a right-handed bottom quark, while Q_4 is the exotic top quark discovered at the Tevatron:

$$\text{Standard Model:} \begin{pmatrix} t \\ b \end{pmatrix}_L b_R, t_R$$

$$\text{exotic model: } \begin{pmatrix} t \\ b \end{pmatrix}_L \begin{pmatrix} Q_1 \cos \Theta_b + b \sin \Theta_b \\ Q_4 \end{pmatrix}_R .$$

It has been shown that fits with data of $Z \to l^+l^-$ and $Z \to b\bar{b}$ processes can be performed assuming a top quark mass of $m_t = 274 \pm 40 \, \text{GeV}$, that would be why it has not been detected yet.

At the Tevatron, the exotic quark has been excluded at a confidence level of 92% [42, 43].

4.2 Techniques Of Top Quark Electric Charge Measurement

4.2.1 Direct Measurement Of the Top Quark Electromagnetic Coupling Through Photon Radiation

One technique to measure the electric charge of the top quark is based on the direct measurement of the top quark electromagnetic coupling through photon radiation in $t\bar{t}$ events.

The radiation of photons off the top quark can be divided into two classes:

- Radiative top quark production: $pp \to t\bar{t}\gamma$

- Radiative top quark decay: $pp \to t\bar{t} \to b\bar{b}W^+W^-\gamma$

In the radiative top quark production the top quark is considered to be stable. This means that the photon is emitted from a virtual top quark. In the radiative top quark decay only the emission of a photon from a on-mass-shell top quark or one of its decay products is taken into account. The separation of the radiative top quark production and the radiative top quark decay is only possible using the narrow width approximation for the top quark. Due to the much higher mass of the top quark compared to the masses of its decay particles, the approximation takes the initial and final state particles of a given subprocess as on-mass-shell ones. Off-shell effects and interference effects between the subprocesses are neglected in this assumption.

In the radiative top quark production, top quark pairs are produced either via gluon fusion or quark anti-quark annihilation. In gluon fusion processes, the photon can be radiated off one of the top quarks (Figure 4.1, upper row). In case of quark anti-quark annihilation, the photon can be emitted by the top quark, antitop quark or one of the incoming quarks (Figure 4.1, lower row). In both cases, the narrow width approximation considers the top quark pair in the final state as on-mass-shell particles. As the gluon fusion dominates at the LHC, the cross section of the radiative top quark production phase should be approximately proportional to Q_t^2.

In radiative top quark decay processes, the situation is more complicated. The photon can be emitted by one of the on-mass-shell top quarks, but also by one of the b quarks or W bosons (Figure 4.2). In the latter case, the coupling is not sensitive to the electric charge of the top quark. These subprocesses cannot be disentangled from the subprocesses sensitive to the top quark electric charge. This results in a cross section for the radiative top quark decay, which is not exclusively proportional to Q_t^2, but still depending on Q_t.

It is experimentally impossible to distinguish between the radiative top quark production and the radiative top quark decay. Only full $t\bar{t}\gamma$ events can be detected, determined by their 7-particle final state (pp→$t\bar{t}(\gamma)$ →b$\bar{b}$q$_1\bar{q}_2$l$^\pm\bar{\nu}_l\gamma$, see Section 2.7). As these events feature either the radiative top quark production or the radiative top quark decay, the cross section should show a Q_t dependence.
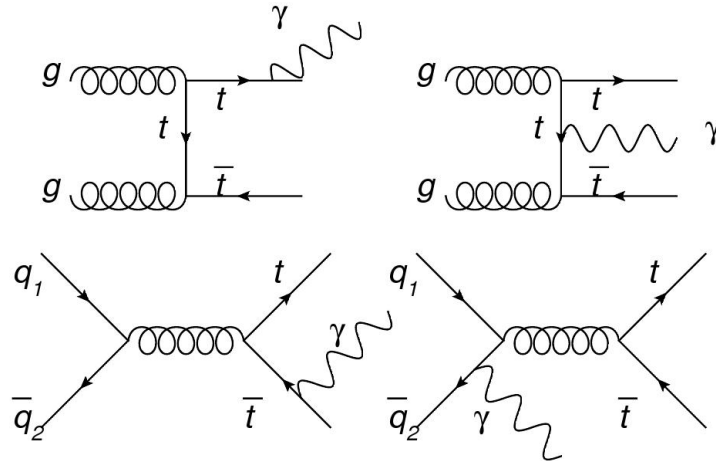
Figure 4.1: Exemplary Feynman diagrams of the radiative top quark production. In the gluon fusion processes (upper row), the photon can be radiated off the $t\bar{t}$ pair (left) or a virtual top quark (right). In case of quark antiquark annihilation (lower row), the photon can be emitted by the top quark (left) or by the initial quarks (right).
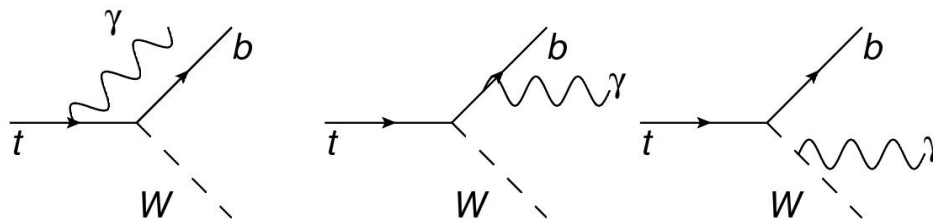
Figure 4.2: Exemplary Feynman diagrams of the radiative top quark decay: The photon can be radiated off the top quark (left diagram), or its decay particles, a W boson (middle diagram) or a bottom quark (right diagram).

4.2.2 Electric Charge Measurement Of The Top Quark Decay Products

The electric charge of the top quark can also be determined by the electric charges of its decay products, a W boson and a bottom quark [45]. The electric charge of the W boson can be determined by its leptonic decay products, while the measurement for the bottom quark is more complex: As the bottom quark hadronizes, a correlation between the electric charge of the b-quark and the electric charges of the hadrons in the b-jet has to be found. The electric charge of the b-jet can be reconstructed via the weighting

technique

$$Q_{bjet} = \frac{\sum_i^N q_i |\vec{j} \cdot \vec{p}_i|^\kappa}{\sum_i^N |\vec{j} \cdot \vec{p}_i|^\kappa},$$

with N charged particles inside the b-jet, q_i and $\vec{p}_i$ being the charge and momentum of the ith particle in the b-jet, $\vec{j}$ the b-jet direction, and κ a free variable. The two possible top quark electric charges lead to an opposite association of the charged lepton and b-jet coming from the same top quark (SM: t→W$^+$b→l$^+\nu$b, exotic: t→W$^-$b→l$^-\nu$b), it has to be distinguish between the association of the b-jet with l$^+$ and and with l$^-$.

Due to low statistic of t$\bar{t}\gamma$ events, the Tevatron collaborations have only performed the top quark charge measurement indirectly via the b-jet charge. As the LHC is expected to produce millions of t$\bar{t}$ events per year, a suffecent number of t$\bar{t}\gamma$ events will be generated for the direct measurement via photon coupling.

4.3 WHIZARD

4.3.1 Overview

For the efficient calculation of the multi-particle scattering cross sections and the generation of events, the Monte Carlo generator WHIZARD (W, HIggs, Z, And Respective Decays) [46, 47] is used. Unlike Monte-Carlo generators as PYTHIA [48] and HERWIG [49], which contain hard-coded libraries of leading-order on-shell matrix elements for simple elementary scattering, decay, and radiation processes, WHIZARD can correctly handle off-shell amplitudes, multi-particle elementary processes and dominant radiative corrections. The theoretical framework is set by leading-order perturbation theory, i.e. tree-level matrix elements, which are calculated fully automatically. The physics described by WHIZARD is conform with the Standard Model, but also includes well-known extensions like the the minimal supersymmetric Standard Model or anomalous couplings. This package does not contain a fixed library of physics processes and it is not limited to a small number of particles at the hard scattering level. For any process that is possible in the selected physics model, the matrix element is computed, using the O'MEGA matrix element generator [50, 47].

O'MEGA is designed to compute helicity amplitudes in the most efficient way by eliminating all redundancies in the calculation as they would show up in a naive Feynman-graph expansion. It implements an algorithm that collects all common subexpressions in the sum over Feynman diagrams contributing to a given scattering amplitude at tree level. The building blocks used in O'MEGA amplitudes correspond to expectation values of fields in states of on-shell external particles. In the case of gauge bosons, they satisfy Ward identities, that ensure that gauge cancellations take place inside these building blocks.

WHIZARD provides code that accounts for suitable phase-space parameterizations, selecting among the multitude of possible channels that integrates and samples phase space in order to generate a sequence of unweighted scattering events. For computing the total cross section, the matrix element returned by O'MEGA has to be integrated over all final-state momenta and also over the initial-parton distributions. For multi-dimensional integration, WHIZARD makes use of the VAMP integration package. This algorithm intro-

duces a multi-dimensional rectangular grid in the integration region, distributing a given number of events among the cells on random basis for each iteration. After several adaptive iterations have resulted in reasonably stable VAMP integration grids and a number of final iterations have yielded a reliable total cross section, events can be generated.

The used sets of parton density functions are provided by the external library LHAPDF (Les Houches Accord PDF) [51].

The overall structure of WHIZARD is shown in Figure 4.3.
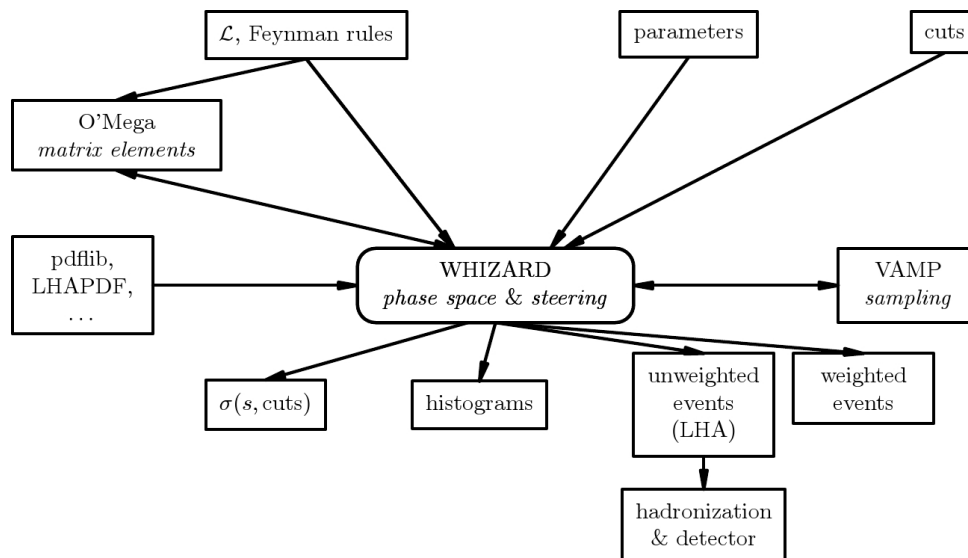
Figure 4.3: Overall structure of WHIZARD [46].

4.3.2 Individual Settings

By defining the two initial and the multiple final state particles, WHIZARD considers every possible process in the cross section calculation, including all constructive and destructive interferences. Therefore, intermediate states are not constrained. Semileptonic $t\bar{t}$ events result in pp$\rightarrow$b$\bar{\text{b}}$q$_1\bar{\text{q}}_2$l$^\pm\bar{\nu}_l$ final state, but also other processes like pp$\rightarrow$W$^+$W$^-$Z can produce the same final state. WHIZARD samples the full phase space of all channels leading to the same final state.

In the sample generation for this thesis, gluons and all quarks, except the top quark, are considered as initial particles. For all calculations, the set CTEQ6 has been used for the parton density functions. The default settings of WHIZARD have been used for the particle masses:

- massless: gluons, light quarks(up, down, charm, strange), electron and all neutrinos

- bottom quark: $m_b = 4.2\,\text{GeV}$

- top quark: $m_t = 174\,\text{GeV}$

- W boson: $m_W = 80.419\,\text{GeV}$

- Muon: $m_\mu = 105.7\,\mathrm{MeV}$

The energy scale has been set to

$$Q^2 = m_t^2$$

Hence, the strong coupling has been recalculated (see section 2.3.1) for this Q^2 with a result of

$$\alpha_s = 0.10643$$

4.4   Comparison Between Possible Top Quark Electric Charges

The analysis of both possible top quark electric charges has been performed on parton level at different stages of the radiative top quark process:

1. $pp \rightarrow t\bar{t}\gamma$

2. $pp \rightarrow b\bar{b}W^+W^-\gamma$

3. $pp \rightarrow b\bar{b}q_1\bar{q}_2 l^\pm \nu_l \gamma$

First, the 3-particle final state is discussed, which is the radiative top quark production process. As mentioned before, the photons are most likely radiated off a top quark, leading to a strong Q_t^2 dependence in the cross section.

In the second process, the top quarks have decayed into W bosons and bottom quarks, resulting in a 5-particle final state. This process is basically the sum of all 5-particle final state processes featuring either the radiative top quark production with the subsequent decay of the top quark or the radiative top quark decay process, with the cross section depending on the top quark electric charge.

In the last step, both W bosons have decayed, one hadronically and the other one leptonically, resulting in 7-particle final state. While the leptons in the final state are an electron or a muon plus a neutrino, both quarks have to be members of the same family, as WHIZARD uses a unitary CKM matrix. Due to the large top quark mass, it is kinematically impossible for the W boson to decay into a top quark and a bottom quark. Therefore the third quark family is excluded.

4.4.1   Cross Sections

Cross sections have been calculated for the 3-, 5- and 7-particle final states.

3-particle and 5-particle final state

For the 3-particle and 5-particle final state, two kinematic cuts have been applied for the photons:

- $|\eta| < 3.5$

- $p_T > 10\,\text{GeV}$

These cuts ensure a good identification of the photons in the ATLAS detector regarding the geometry and energy resolution of the detector.

Cross section have been calculated for a center of mass energy of 10 TeV and 14 TeV and the results are listed in Tables 4.1 and 4.2. Also listed are the cross sections for the corresponding processes without photon radiation, showing equal results for the Standard Model and the exotic top quark model. These values verify that differences between the two possible top quark electric charges do not occur in non-radiative processes.

The 3-particle final state shows a significant difference between the total cross sections of both top quark models. The total cross section $\sigma_{t,ex}$ for the exotic top quark model is (2.85±0.03) times larger than the result for the Standard Model at a center of mass energy of $\sqrt{s} = 10\,\text{TeV}$. For $\sqrt{s} = 14\,\text{TeV}$ the ratio of both cross sections is even higher with (3.14±0.01). If photons are exclusively radiated off top quarks, the cross sections are expected to be proportional to Q_t^2 resulting in a ratio of both top quark models of $(\frac{-4}{3})^2/(\frac{2}{3})^2 = 4$. The calculated ratios are smaller than 4, because photons can also be emitted from initial quarks (see Section 4.2). This process is not sensitive to the electirc charge of the top quark. But the results show that the gluon fusion processes are the dominant top quark production channels, even more dominant for higher energies due to the behaviour of the parton density functions (see Section 2.6).

In the 5-particle final state process, the calculated cross section for the exotic quark is (1.49±0.01) times higher than for the Standard Model top quark at a center of mass energy of $\sqrt{s} = 10\,\text{TeV}$ and (1.61±0.01) higher at $\sqrt{s} = 14\,\text{TeV}$. The ratios are smaller than those for the 3-particle final state, because photons in the radiative top quark decay can also be emitted from a W boson or a bottom quark. In addition there are interference terms in the radiative top quark decay. As these interferences are constructive for $Q_t = \frac{2}{3}$ and destructive for $Q_t = -\frac{4}{3}$, the cross section for the radiative top quark decay is smaller in the exotic model than for the Standard Model (see Table 4.4). This results in much smaller ratio of the cross section for the 5-particle final state than for the 3-particle final state.

process	$Q_t = \frac{2}{3}$ $\sigma_{t,sm}$ [pzb]	$Q_t = -\frac{4}{3}$ $\sigma_{t,xm}$ [pb]	Ratio $\sigma_{t,sm}/\sigma_{t,xm}$
pp→t$\bar{\text{t}}$	217.71±0.93	218.73±0.87	1.00±0.01
pp→t$\bar{\text{t}}\gamma$	1.08±0.01	3.08±0.01	2.85±0.03
pp→b$\bar{\text{b}}$W$^+$W$^-$	230.98±0.56	233.37±0.67	1.01±0.01
pp→b$\bar{\text{b}}$W$^+$W$^-\gamma$	2.58±0.01	3.85±0.01	1.49±0.01

Table 4.1: Calculated cross-sections σ_t for radiative and non-radiative top quark subprocesses at $\sqrt{s} = 10\,\text{TeV}$. Results are shown for the two top quark models.

process	$Q_t = \frac{2}{3}$ $\sigma_{t,sm}$ [pb]	$Q_t = -\frac{4}{3}$ $\sigma_{t,xm}$ [pb]	Ratio $\sigma_{t,sm}/\sigma_{t,xm}$
pp→t$\bar{\text{t}}$	496.34±2.10	496.89±2.36	1.00±0.01
pp→t$\bar{\text{t}}\gamma$	2.43±0.01	7.63±0.03	3.14±0.02
pp→b$\bar{\text{b}}$W$^+$W$^-$	521.43±1.34	529.48±1.49	1.02±0.01
pp→b$\bar{\text{b}}$W$^+$W$^-\gamma$	5.86±0.02	9.41±0.03	1.61±0.01

Table 4.2: Calculated cross-sections σ_t for radiative and non-radiative top quark subprocesses at $\sqrt{s} = 14\,\text{TeV}$. Results are shown for the two top quark models.

7-particle final state

For the 7-particle final state, no kinematic cuts could explicitly be applied to the photons due to calculation issues of WHIZARD. For the momenta of massless particles default cuts have been set by WHIZARD:

- $p_\gamma > 10\,\text{GeV}$

- $p_e > 10\,\text{GeV}$

- $p_\nu > 10\,\text{GeV}$

Thus, a momentum cut has been applied for electrons in the final state, but no cut could been set for muons in the final state, for the same reasons as for the photons.

The results of the cross section calculation are listed in Table 4.3.

The cross-section ratio of the exotic and the Standard Model top quark electric charge is smaller than for the 5-particle final state with (1.28±0.01) for the electron channel and (1.20±0.01) for the muon channel. This can be explained with the additional particles from the W decays, the quark pair and the charged lepton, which can emit a photon, but are not sensitive to the top quark charge. This also results in interference terms which are only constructive for the Standard Model. The difference in the cross section between the electron channel and the muon channel can be partially explained by the higher momentum cut for electrons.

process	$Q_t = \frac{2}{3}$ $\sigma_{t,sm}$ [fb]	$Q_t = -\frac{4}{3}$ $\sigma_{t,xm}$ [fb]	Ratio $\sigma_{t,sm}/\sigma_{t,xm}$
pp→b$\bar{\text{b}}$ud̄e$^-\bar{\nu}_e\gamma$	197.52±0.44	255.72±0.95	1.29±0.01
pp→b$\bar{\text{b}}$cs̄e$^-\bar{\nu}_e\gamma$	198.84±0.52	252.64±0.77	1.27±0.01
pp→b$\bar{\text{b}}$dū e$^+\nu_e\gamma$	198.98±0.34	257.27±0.79	1.29±0.01
pp→b$\bar{\text{b}}$sc̄e$^+\nu_e\gamma$	199.41±0.42	255.55±0.79	1.28±0.01
pp→b$\bar{\text{b}}$q$_1$q̄$_2$e$^\pm\nu_e\gamma$	794.75±1.72	1021.18±3.30	1.28±0.01
pp→b$\bar{\text{b}}$ud̄$\mu^-\bar{\nu}_\mu\gamma$	456.26±1.59	547.17±1.85	1.20±0.01
pp→b$\bar{\text{b}}$cs̄$\mu^-\bar{\nu}_\mu\gamma$	449.28±1.49	537.66±1.47	1.20±0.01
pp→b$\bar{\text{b}}$dū$\mu^+\nu_\mu\gamma$	456.40±1.67	549.88±1.87	1.20±0.01
pp→b$\bar{\text{b}}$sc̄$\mu^+\nu_\mu\gamma$	454.72±1.58	549.32±1.70	1.21±0.01
pp→b$\bar{\text{b}}$q$_1$q̄$_2\mu^\pm\nu_\mu\gamma$	1816.66±6.33	2184.03±6.89	1.20±0.01

Table 4.3: Calculated cross-sections for 7-particle final state processes with e$^\pm$ or $\mu^\pm$ in the final state at $\sqrt{s} = 10$ TeV

4.4.2 Kinematic Distributions

For the comparison of the different kinematic distributions of the Standard Model and the exotic top quark charge, 100,000 events have been generated for each of the 3-particle 5-particle and 7-particle final state processes at a center of mass energy of $\sqrt{s} = 10$ TeV. As it is expected that distributions regarding the top quark are equal to distributions regarding the antitop quark, the results of both quarks are combined into one histogram, resulting in two entries per event.

Even though the cross section for the two models is different, only the shape of the distributions is considered in this analysis. Especially in the first year of data taking, the measured absolute cross sections will have large systematic uncertainties. It will be therefore difficult to distinguish between the two models just by measuring the cross section. Therefore the main aim of this chapter is the comparison of shapes of distributions. For this purpose the hoistograms are not normalized to the expected cross section, but to the same numbers of events.

3-particle final state

The distributions of the 3-particle final state process can be seen in Figures 4.4 to 4.7. Only minor differences can be observed in the shape comparison of each distributions:

- The η distributions of the emitted photon (Figure 4.4) and the top quark (Figure 4.7) show a slightly narrower distribution for the exotic top quark distribution than for the Standard model top quark.

- The distribution of the minimum angle between the photon and the top quark (Figure 4.6, right) shows more entries for the exotic top quark distribution in an angle range of 0.5 rad to 1.5 rad than the Standard Model distribution.
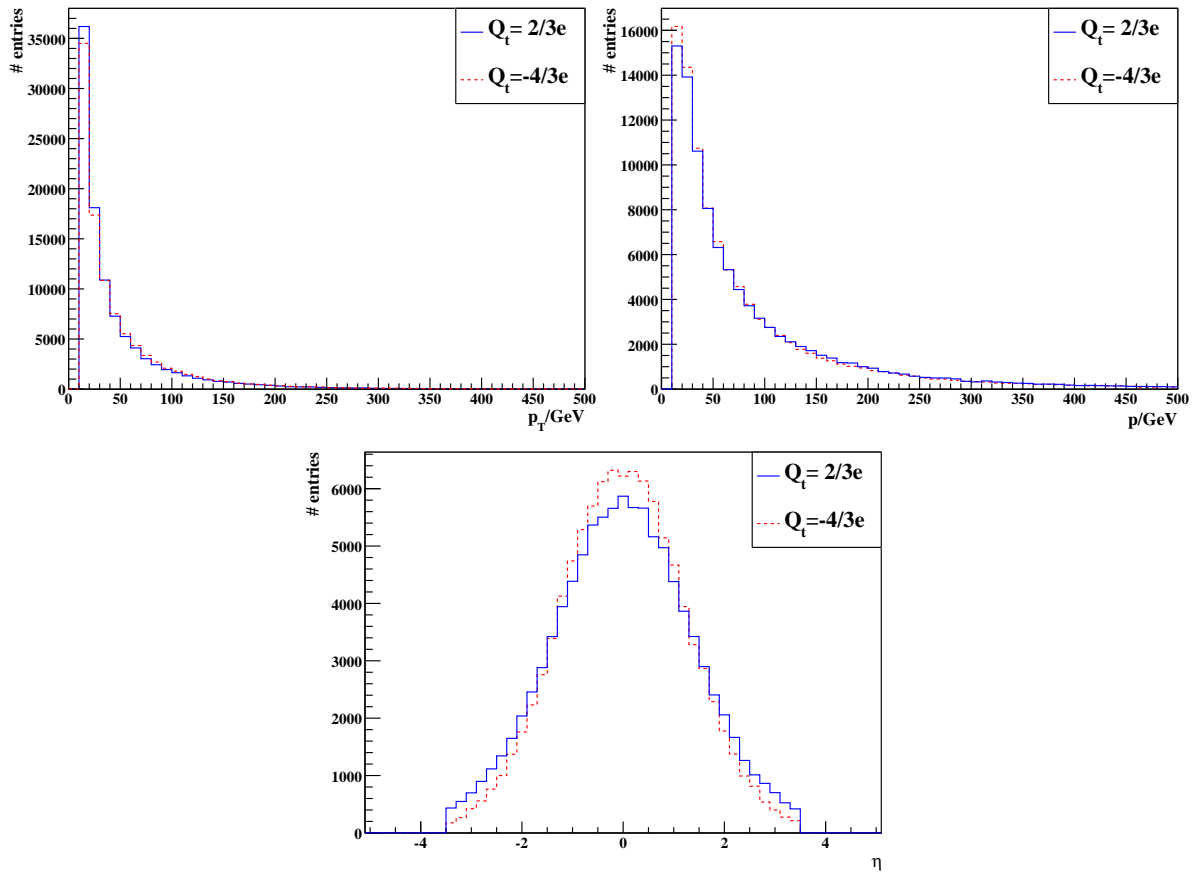
Figure 4.4: pp→t$\bar{\text{t}}$γ: p$_T$ (upper left), $|\vec{p}|$ (upper right) and η-distributions (lower row) of the photon for the Standard Model (solid lines) and the exotic top quark model (dashed lines).
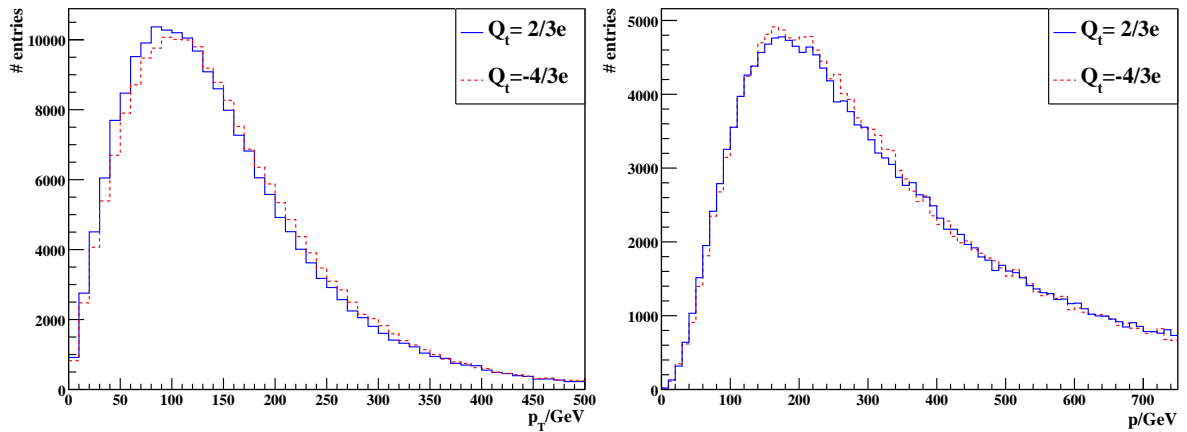
Figure 4.5: pp→t$\bar{\text{t}}$γ: p$_T$ (left) and $|\vec{p}|$ distributions (right) of the top quark for the Standard Model (solid lines) and the exotic top quark model (dashed lines).
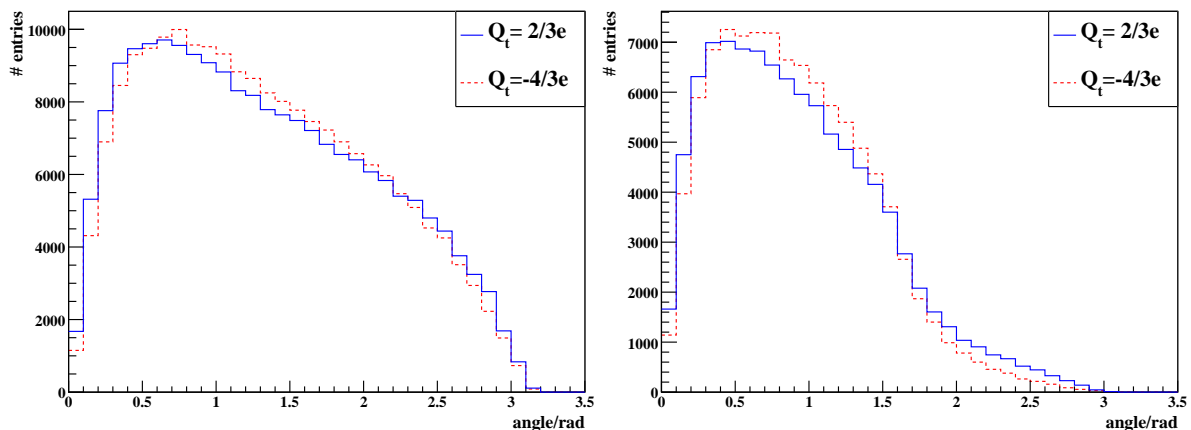
Figure 4.6: pp→t$\bar{\text{t}}$γ: Angular distributions of the opening angle between the photon and the top quark for the Standard Model (solid lines) and the exotic top quark model (dashed lines). On the left, the histogram shows the distribution of the angle between the photon and both the top and antitop quark, while the distribution on the right shows only the minimum of the two angles in each event.
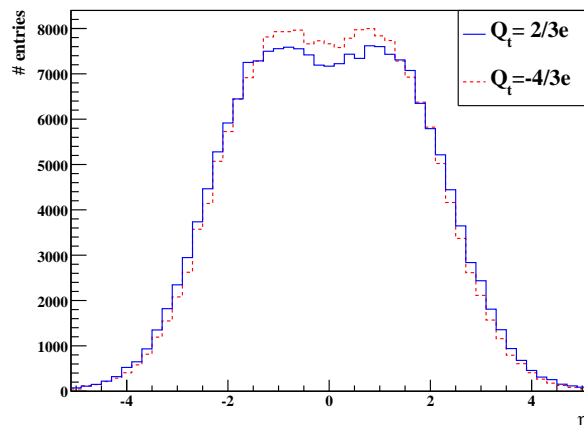
Figure 4.7: pp→t$\bar{\text{t}}$γ: η distribution of the top quark for the Standard Model (solid lines) and the exotic top quark model (dashed lines).

5-particle final state

The kinematic distributions of the 5-particle final state are shown in Figures 4.8 to 4.13. As the top quark and the antitop quark are not part of the final state, their momenta have to be reconstructed with their respective decay products. Different cases have to be considered:

- The top quark decays differently for the two top quark models:

  - Standard Model: t→W$^+$b , $\bar{\text{t}}$ →W$^-$b
  - Exotic model: t→W$^-$b , $\bar{\text{t}}$ →W$^+$b

- It cannot be distinguished whether the photon is emitted during the top quark production process or top quark decay process. Hence, both cases have to be respected.

Therefore, the reconstruction of the top quark momenta is done in the following ways:

1. Standard Model: $\vec{p}(t)=\vec{p}(W^+)+\vec{p}(b)$, $\vec{p}(\bar{t})=\vec{p}(W^-)+\vec{p}(\bar{b})$
   Exotic: $\vec{p}(t)=\vec{p}(W^-)+\vec{p}(b)$, $\vec{p}(\bar{t})=\vec{p}(W^+)+\vec{p}(\bar{b})$

2. Standard Model: $\vec{p}(t)=\vec{p}(W^+)+\vec{p}(b)+\vec{p}(\gamma)$, $\vec{p}(\bar{t})=\vec{p}(W^-)+\vec{p}(\bar{b})+\vec{p}(\gamma)$
   Exotic: $\vec{p}(t)=\vec{p}(W^-)+\vec{p}(b)+\vec{p}(\gamma)$, $\vec{p}(\bar{t})=\vec{p}(W^+)+\vec{p}(\bar{b})+\vec{p}(\gamma)$

The first method assumes that the photon is emitted from a virtual top quark, i.e. during the top quark production, while the second method assumes that the photon is part of the top quark decay. A few shape differences can be observed between the distributions of both top quark models:

- The $|\vec{p}|$ and p_T distributions of the emitted photons (Figure 4.8) show higher maxima at their respective minimum values of $10\,\text{GeV}$ for the Standard Model distributions, while the exotic top quark distribution shows a slightly narrower distribution in the η histogram.

- The η distributions of the top quark (Figure 4.9) show less entries for the exotic top quark distributions in the range of $|\eta| > 1.5$.

- The $|\vec{p}|$ and p_T distributions of the top quark are shown in Figure 4.10. In all histograms, the exotic top quark charge distributions show smaller maxima, which are shifted to slightly higher momentum values compared to the Standard Model distributions.

- The angular distributions of the opening angle between the photon and the top quark (Figure 4.11) show for the exotic top quark distributions a slight shift of the maxima towards larger angles as well as smaller maxima compared to the distibutions of the Standard Model top quark. Further, the exotic top quark distributions have a constant slope in an angle range of $0.7\,\text{rad}$ to $2.4\,\text{rad}$, while the Standard Model distributions show a decreasing slope in this range.

- The angular distributions of the opening angle between the photon with the W boson (Figure 4.13, left) show a smaller maximum for the exotic top quark distribution, but rather more entries in a range of $0.9\,\text{rad}$ to $2.4\,\text{rad}$ than the Standard model distribution.

- The angular distributions of the opening angle between the photon and the bottom quark (Figure 4.13, right) show significant differences between both top quark models. The distribution of the exotic quark incline up to a maximum at around $1\,\text{rad}$ and then decrease with an increasing gradient, while the Standard Model distibutions decrease above an angle of $0.8\,\text{rad}$ without developing a visible maximum.

The angular distributions of the opening angle between the top quark and its assigned decay particles show almost identical distributions for both top quark models (Figure 4.12).
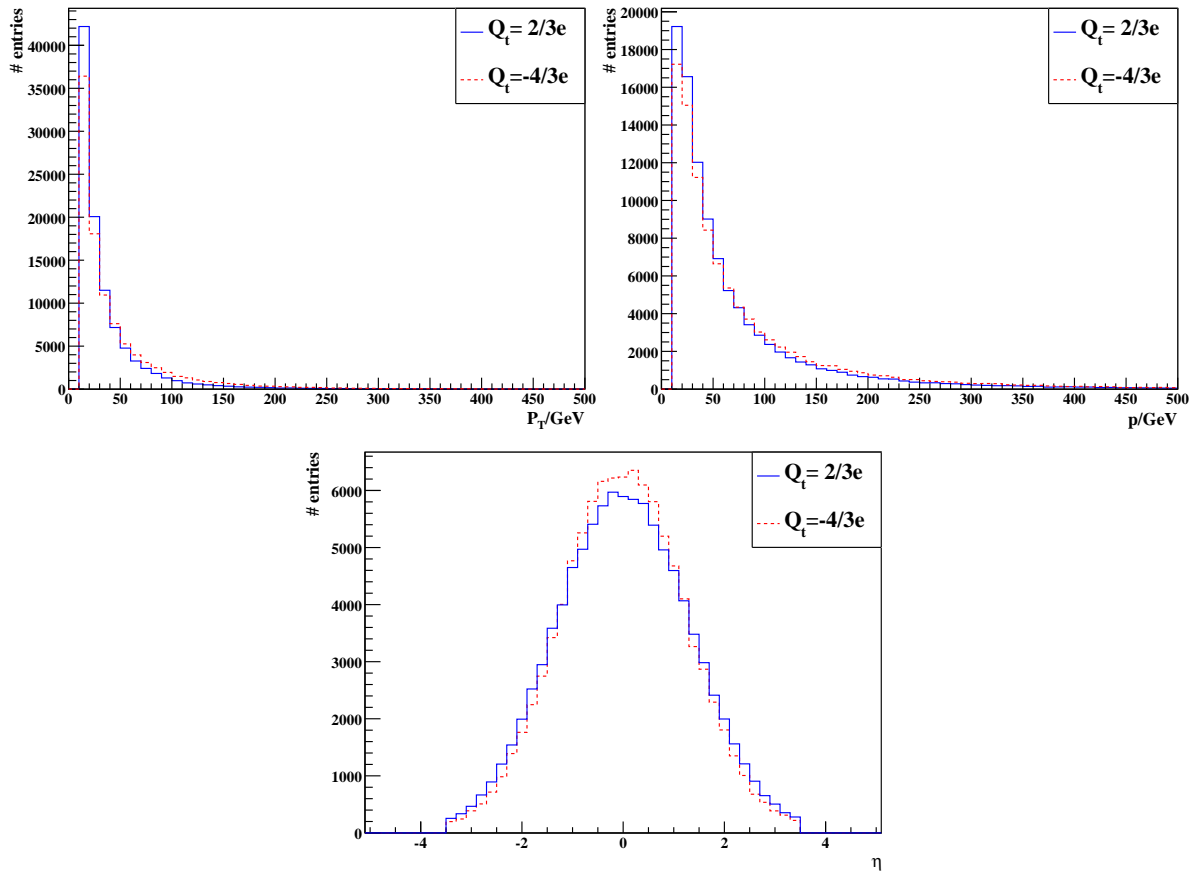
Figure 4.8: pp→b$\bar{\text{b}}$W$^+$W$^-\gamma$: p$_T$ (upper left), $|\vec{p}|$ (upper right) and η distributions (lower row) of the photon for the Standard Model (solid lines) and the exotic top quark model (dashed lines).
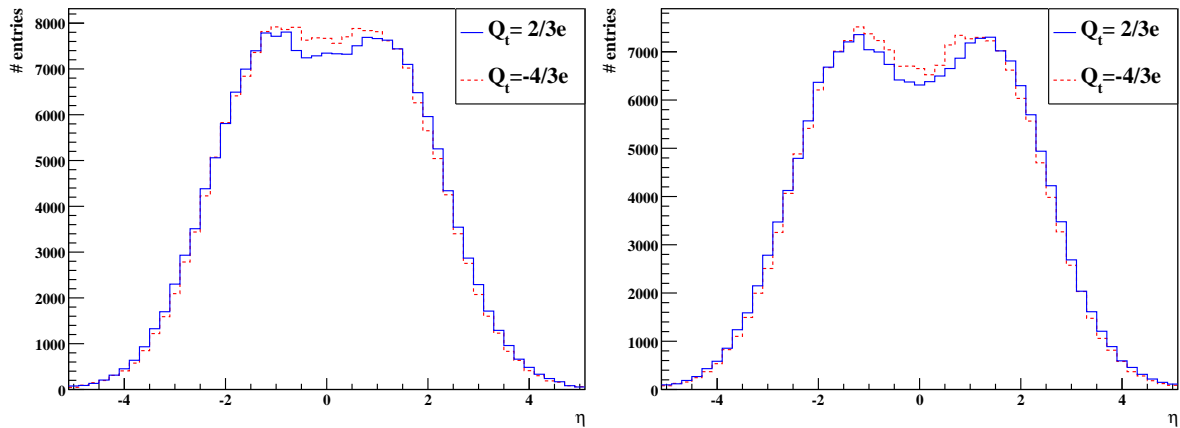
Figure 4.9: pp→b$\bar{\text{b}}$W$^+$W$^-\gamma$: η distributions of the top quark for the Standard Model (solid lines) and the exotic top quark model (dashed lines). In the histogram on the left, the photon is ignored in the reconstruction of the top quark momentum in the left histogram, while in the distributions on the right, the photon is included in the reconstruction.
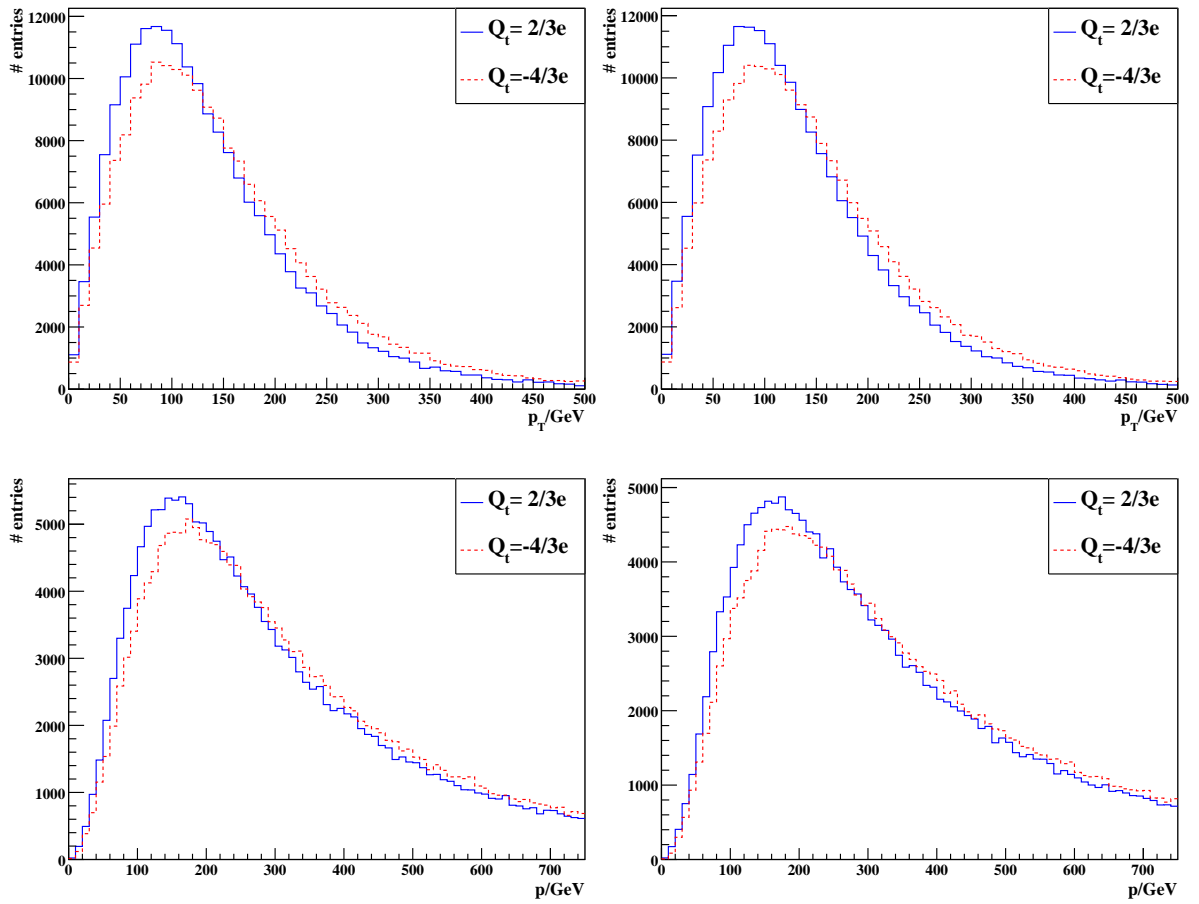
Figure 4.10: pp→b$\bar{\text{b}}$W$^+$W$^-\gamma$: p$_\text{T}$ (upper row) and $|\vec{p}|$ distributions (lower row) of the top quark for the Standard Model (solid lines) and the exotic top quark model (dashed lines). In both rows, the photon is ignored in the reconstruction of the top quark momentum in the left histogram, while in the distributions on the right, the photon is included in the reconstruction.
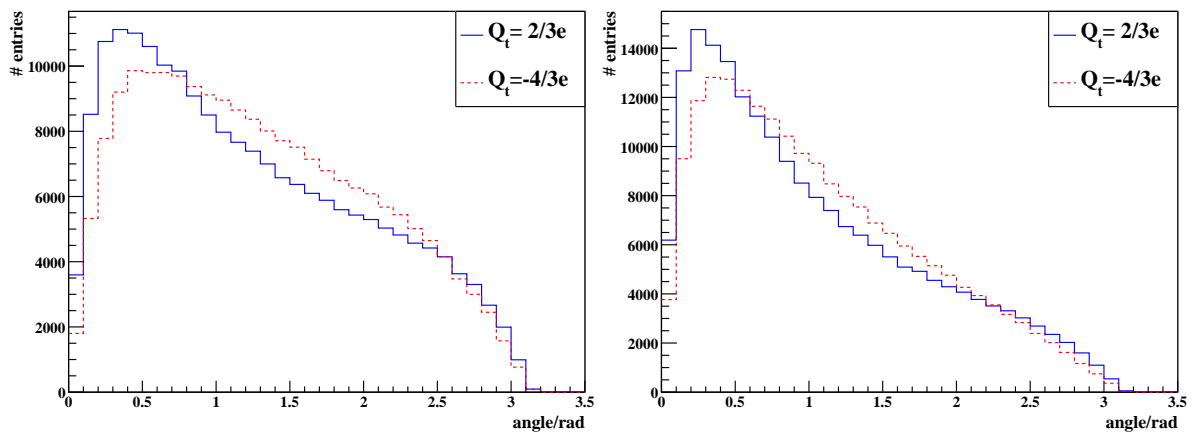
Figure 4.11: pp→b$\bar{\text{b}}$W$^+$W$^-\gamma$: angular distributions of the opening angle between photon and the top quark for the Standard Model (solid lines) and the exotic top quark model (dashed lines). In the histogram on the left, the photon is ignored in the reconstruction of the top quark momentum, while in the distributions on the right, the photon is included in the reconstruction.

Figure 4.12: pp→b̄bW⁺W⁻γ: angular distributions of the opening angle between the top quark and its assigned decay particles for the Standard Model (solid lines) and the exotic top quark model (dashed lines). The histograms in the upper row show the angular distributions between the top quark and the W boson, while in the lower row, the angular distributions between the top quark and the bottom quark are presented. In both rows, the photon is ignored in the reconstruction of the top quark momentum in the left histograms, while in the distributions on the right, the photon is included in the reconstruction.

Figure 4.13: pp→b̄bW⁺W⁻γ: angular distributions of the opening angle between the photon and either the W boson (left) or the bottom quark (right) for the Standard Model (solid lines) and the exotic top quark model (dashed lines).

4.4.3 Invariant Mass Distributions

5-particle final state

For the 5-particle final state processes, the invariant mass of the top quark has been calculated for each event. The distributions of the resulting values are presented in Figure 4.14. Like for the top quark momentum, two different methods of the invariant mass calculation have to be considered which either include or exclude the photon in the calculations:

1. Standard Model: $m(t) = \sqrt{(E(W^+) + E(b) + E(\gamma))^2 - (\vec{p}(W^+) + \vec{p}(b) + \vec{p}(\gamma))^2}$
   $m(\bar{t}) = \sqrt{(E(W^-) + E(\bar{b}) + E(\gamma))^2 - (\vec{p}(W^-) + \vec{p}(\bar{b}) + \vec{p}(\gamma))^2}$

   Exotic: $\quad m(t) = \sqrt{(E(W^-) + E(b) + E(\gamma))^2 - (\vec{p}(W^-) + \vec{p}(b) + \vec{p}(\gamma))^2}$
   $m(\bar{t}) = \sqrt{(E(W^+) + E(\bar{b}) + E(\gamma))^2 - (\vec{p}(W^+) + \vec{p}(\bar{b}) + \vec{p}(\gamma))^2}$

2. Standard Model: $m(t) = \sqrt{(E(W^+) + E(b))^2 - (\vec{p}(W^+) + \vec{p}(b))^2}$
   $m(\bar{t}) = \sqrt{(E(W^-) + E(\bar{b}))^2 - (\vec{p}(W^-) + \vec{p}(\bar{b}))^2}$

   Exotic: $\quad m(t) = \sqrt{(E(W^-) + E(b))^2 - (\vec{p}(W^-) + \vec{p}(b))^2}$
   $m(\bar{t}) = \sqrt{(E(W^+) + E(\bar{b}))^2 - (\vec{p}(W^+) + \vec{p}(\bar{b}))^2}$

Significant differences between both top quark models can be observed in these invariant mass distributions.

For the first method, which includes the photon in the reconstruction, two peaks are visible in the invariant mass distributions which can be explained by the two processes of the radiative top production and top decay:

- The first peak is located at the rest mass of the top quark. The invariant mass can only be equal to the rest mass of the top quark, if the photon is radiated off the on-mass-shell top quark or one of its two decay particles, the W boson or the bottom quark. Therefore events, which form the top quark mass peak, have to be 5-particle final state processes with the photon radiation during the top decay phase. Furthermore, it can be observed that the peak is about 3.5 times higher for the Standard Model distribution than for the exotic top quark distribution. This implies that the number of entries at the peak agrees with the results in section 4.4.1, which show a smaller cross section for the radiative top quark decay for the exotic model than for the Standard Model.

- Above the top quark mass, a second, much broader peak can be observed with a maximum at around $190\,\mathrm{GeV}$. If the photon is emitted in the top quark production process, the invariant mass of the W boson and the bottom quark should be equal to the top quark mass of $174\,\mathrm{GeV}$. But the additional particle in the calculation leads to an invariant mass above the rest mass of the top quark. Hence, the second peak correspond to the radiative top quark production. This peak is more distinctive for the exotic model which agrees with the much higher cross section of the top quark production process for the exotic top quark than for the Standard Model top quark (see section 4.3).

For the second method, which does not consider the photon in the reconstruction, the distributions are basically single peaks at the top mass of 174 GeV. Only a small tail is visible below the top quark mass for both top quark models. In this case, the top quark mass is reconstructed by the W boson and the bottom quark, indicating that the photon has to be emitted during the top production phase. Therefore, the top mass peak corresponds in these distributions to the radiative top quark production.
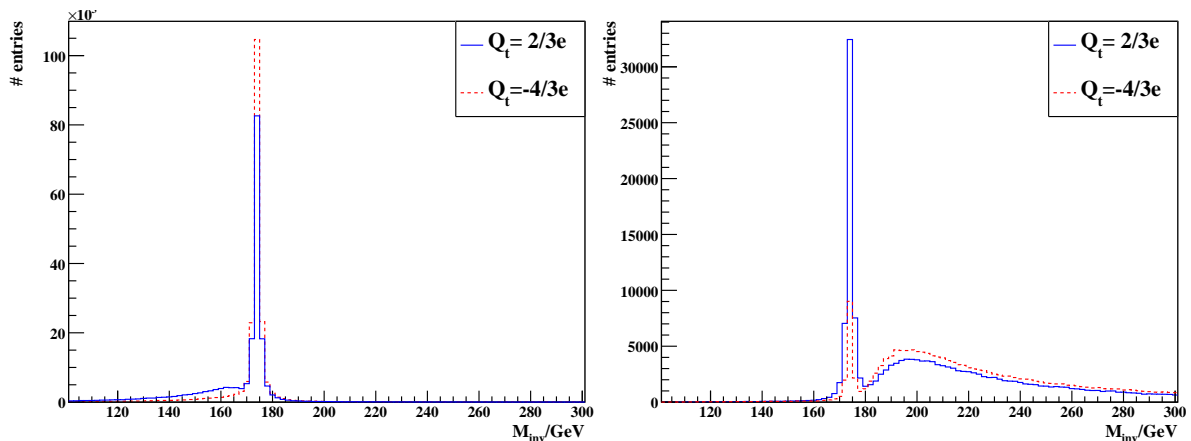
Figure 4.14: pp→b$\bar{\text{b}}$W$^+$W$^-\gamma$: invariant mass distributions of top quark for the Standard Model (solid lines) and the exotic top quark model (dashed lines). In the histogram on the left, the photon is ignored in the calculation of the invariant mass, while in the distributions on the right, the photon is included in the calculation.

7-particle final state

In a last step, the invariant mass distributions of the top quark have been calculated for the 7-particle final state processes, focusing on events with electrons as the charged lepton in the final state. In these distributions, it has been distinguished between top quarks regarding their decay modes:

- Hadronic top quark: The top or antitop quark has decayed into a (anti)bottom quark and a W boson, which has decayed into quarks of the first or second family (u$\bar{\text{d}}$, d$\bar{\text{u}}$, c$\bar{\text{s}}$, s$\bar{\text{c}}$)

- Leptonic top quark: The W boson has decayed into an electron and a neutrino (e$^-\bar{\nu}_e$, e$^+\nu_e$)

The histograms (Figure 4.15) show that the invariant mass distributions have mantained their characteristics compared to the distributions of the 5-particle final state, with the peaks corresponding to either the radiative top production or top decay. But differences in the peak height for the two top quark models can be observed regarding the decay modes of the W bosons.

The additional particles lead to new possibilities for the photon to be emitted in the top quark decay. This yields more top quark events featuring the radiative top quark decay

process and therefore higher peaks in the distributions which include the photon in the invariant mass calculation. The shift results in fewer events featuring the radiative top quark production, which is visible in smaller top mass peaks in the distributions excluding the photon. Further, the electron is favored as photon radiator over the two light quarks in the final state. Hence, the top quark mass peak in the distribution, which includes the photon in the invariant mass calculation, is significantly higher for the leptonic top quark than the hadronic top quark.

The hadronic and leptonic top quark are combined in the histograms in Figure 4.16. Overall, the differences between both top quark models are less significant when 7-particle final state events are considered, compared to the 5-particle final state process.
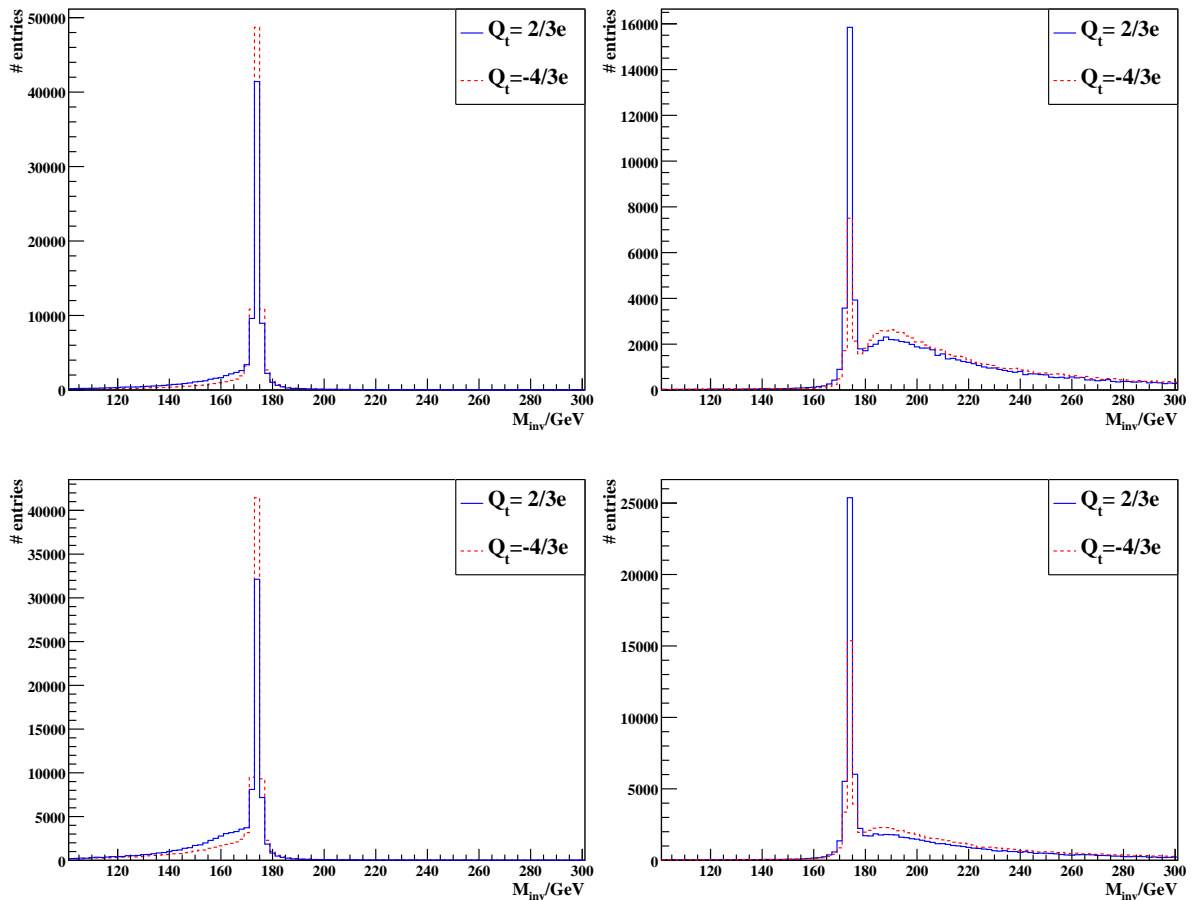
Figure 4.15: $pp \rightarrow b\bar{b}q_1\bar{q}_2 e^{\pm}\nu_e \gamma$: invariant mass distributions of the hadronic top quark (upper row) and leptonic top quark (lower row) for the Standard Model (solid lines) and the exotic model (dashed lines). In both rows, the photon is ignored in the invariant mass calculation in the left histogram, while in the distributions on the right, the photon is included in the calculation.
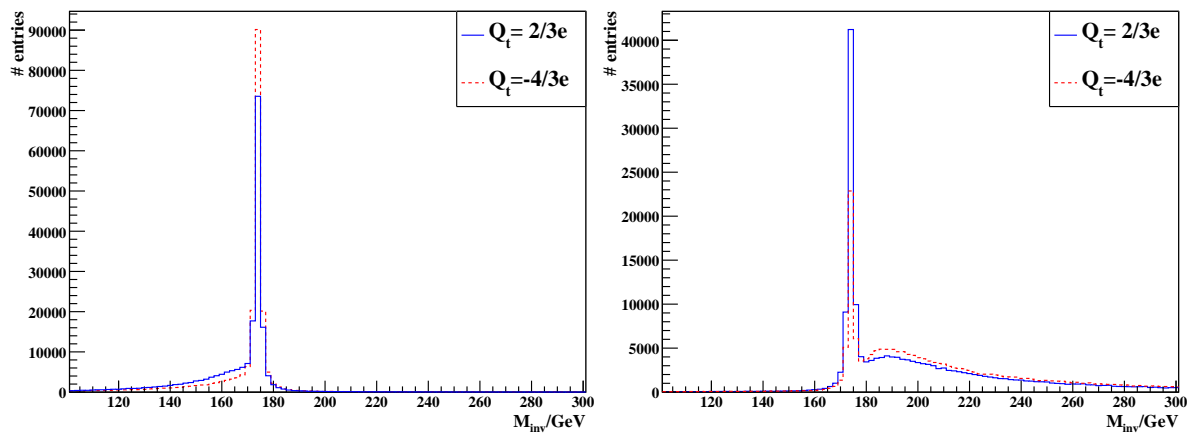
Figure 4.16: pp$\rightarrow$b$\bar{\text{b}}$q$_1$$\bar{\text{q}}_2e^\pm$$\nu_e$$\gamma$: invariant mass distributions of the Standard Model top quark (solid line) and the exotic top quark (dashed line). In the histogram on the left, the photon is ignored in the calculation of the invariant mass, while in the distributions on the right, the photon is included in the calculation.

4.5   Comparison With Previous t$\bar{\text{t}}$$\gamma$ analysis

A first theoretical analysis of determing the top quark charge directly via photon coupling with ATLAS is presented in [45]. In this work, the narrow width approximation is used to factorize the 5-particle final state process into the radiative top quark production and the radiative top quark decay in order to treat them seperately. Due to the much higher mass of the top quark compared with that of the W boson, the approximation is used to take the initial and final state particles of a given subprocess as on-mass-shell ones. The calculated cross sections for both subprocesses at a center of mass energy of $\sqrt{\text{s}} = 14\,\text{TeV}$, as well as their sum, which is the result for the 5-particle final state process are shown in Table 4.4. In the calculations, cuts on η and the transverse momentum of the photon have been applied:

- $|\eta| < 3.5$

- $\text{p}_\text{T} < 10\,\text{GeV}$

	$Q_t = \frac{2}{3}$	$Q_t = -\frac{4}{3}$	Ratio
process	$\sigma_{t,sm}$ [pb]	$\sigma_{t,ex}$ [pb]	$\sigma_{t,sm}/\sigma_{t,ex}$
pp$\rightarrow$t$\bar{\text{t}}$$\gamma$	2.31	7.34	3.18
pp$\rightarrow$t$\bar{\text{t}}$ $\rightarrow$b$\bar{\text{b}}$W$^+$W$^-$$\gamma$	2.96	1.16	0.39
pp$\rightarrow$t$\bar{\text{t}}$(γ) $\rightarrow$bbW$^+$W$^-$$\gamma$	5.27	8.50	1.61

Table 4.4: Results of the cross-section calculation in [45] at $\sqrt{\text{s}} = 14\,\text{TeV}$

As it is experimentally impossible to seperate between the two subprocesses, this theoretical approach is not used in this thesis. Therefore, the result of the radiative top decay

subprocess alone is not reproduced.

The cross sections of the 3-particle and 5-particle final state at $\sqrt{s} = 14\,\text{TeV}$, which are calculated with WHIZARD, are listed again in Table 4.5.

	$Q_t = \frac{2}{3}$	$Q_t = -\frac{4}{3}$	Ratio
process	$\sigma_{t,sm}$ [pb]	$\sigma_{t,xm}$ [pb]	$\sigma_{t,sm}/\sigma_{t,xm}$
pp→t$\bar{\text{t}}\gamma$	2.43±0.01	7.63±0.03	3.14±0.02
pp→b$\bar{\text{b}}$W$^+$W$^-\gamma$	5.86±0.02	9.41±0.03	1.61±0.01

Table 4.5: Results of the cross-section calculation by WHIZARD at $\sqrt{s} = 14\,\text{TeV}$

Comparing the radiative top production cross sections very similar results are achived for the calculations from [45] and this thesis. Deviations can be explained with two differences in the cross section calculations:

- Different parton density functions were used ([45]: CTEQ5, WHIZARD: CTEQ6)

- The QCD scale is given in [45] by the average of the squares of produced top transverse masses ($Q^2 = (m_T(t_1)^2 + m_T(t_2))/2$). As a variable value for the QCD scale is not allowed in WHIZARD, the analysis in this thesis uses the squares of the top quark mass as the QCD scale ($Q^2 = m_t^2$).

The values of the 5-particle final state process, which have been calculated with WHIZARD, show good agreement with the sum of the top production and top decay phase from the previous analysis. The difference for the 5-particle final state of about 10% is larger than that in the radiative top quark production process alone (5%). The reason for this is that there is no constraint in WHIZARD that the W bosons and the bottom quarks are decay products of a t$\bar{\text{t}}$ pair. This results in additional Feynman diagrams with the same final state considered in the phase space calculation.

The ratios of the cross sections for the exotic and the Standard Model top quark electric charge show almost perfect agreement between both analyses. The 3-particle final state gives a ratio of 3.14±0.02 with WHIZARD compared to 3.18 in [45], and for 5-particle final state agreement of 1.61±0.01 to 1.61.

In summary, the reproduction of the results in [45] showed very good agreements and have verified the cross-sections of the radiative top quark processes calculated with WHIZARD.

4.6 Summary

The results in this chapter have shown differences between the Standard Model and the exotic top quark model, presenting the possibilities to distinguish between those two possible electric charges of the top quark.

The Monte Carlo generator WHIZARD has provided the opportunity to calculate the phase space and generate events not only for Standard Model processes, but also for an exotic model with a top quark charge of $-\frac{4}{3}$e.

The cross section calculations have shown big differences between both top quark models in the results for the radiative top quark production. This difference is reduced in processes

including the top quark decay, but is still large enough to provide the opportunity to distinguish between the two models.

As the measurement of the absolute cross section will have large uncertainties in the beginning of the data taking with the ATLAS detector, a method relying on the the shape of the variables rather than the total number of events is investigated. A possibility to differentiate between the Standard Model and the exotic top quark is presented in the invariant mass distributions of the top quark. These distributions feature peaks, which correspond to the radiative top quark production and top quark decay processes, showing the possibility to distinguish between the two processes.

Chapter 5

Electric Charge Measurement Of The Top Quark

The results in the previous chapter were determined using the four vectors of the particles from the Monte Carlo generation. In a next step, Monte Carlo data samples have to be generated, which also take the response of the ATLAS detector into account. The procedure of the Monte Carlo data production is described in Section 5.1. The resulting datasets are summarized in Section 5.2. In Section 5.3 selection cuts have been performed on the data samples in order to choose the 7-particle final state event candidates. In Section 5.4, a method to differenciate between the two top quark models is developed and performed on parton level and detector level for an integrated luminosity of $1\,\mathrm{fb}^{-1}$.

5.1　Full Simulation Monte Carlo Data Production

In order to take the response of the ATLAS detector into account, Monte Carlo data samples have to be generated using the ATLAS computing framework ATHENA [52]. This fully object-oriented software framework is designed for data processing, simulation, reconstruction and physics analysis, providing the user with derived physics objects, e.g. in the form of four-momenta for jets and leptons.

For the $t\bar{t}\gamma$ analysis including detector response, full simulation samples of semileptonic $t\bar{t}\gamma$ processes with an electron as lepton in the final state have been generated (7-particle final state), performed in four separate steps [52]:

- Event generation

- Detector simulation

- Hit digitization

- Reconstruction

The full chain simulation has been performed with ATHENA version 15.0.0 in the following way:
Before including the detector effects, the WHIZARD events are hadronized, as well as

initial state and final state radiation added, which is done by the Monte Carlo program PYTHIA [48] using the parton distribution function CTEQ6L and the ATLAS settings for the official MC08 production [53]. The WHIZARD events are the same ones used in the previous chapter providing the invariant mass distributions for the 7-particle final state. In the second step, the GEANT4 package is used for the ATLAS simulation estimating the response of the detector, which include particle interactions with matter inside the detector and the deflection of particles due to the magnetic field. For all datasets ATLAS-GEO-02-01-00 has been used for the detector description.

In the third production step, energy deposits simulated during the detector simulation process are transformed into signals resembling a realistic simulation of the data provided by the detector's electronics.

The digitized data are passed to the final production process, the reconstruction, which executes algorithms reconstructing physical observables of the event. The output data is stored in the Analysis Object Data (AOD) format, which are used for the physics analysis of this thesis.

The full chain of Monte Carlo data production is shown schematically in Figure 5.1.

Figure 5.1: Schematic representation of the full chain simulation

5.2 Data Samples

Data samples have been produced via the before described full chain production, providing 7-particle final state events, which have been originated in LHC proton-proton collisions with a center of mass energy of $\sqrt{s} = 10\,\text{TeV}$. As this analysis focuses on events with $e^{\pm}$ as charged leptons in the final state, the generated samples include four different final states, as shown in Table 5.1. Therefore, a total of eight different datasets have been produced,

four for each electric charge model of the top quark.

The Tables 5.1 and 5.2 summarize the datasets with their physics signature, amount of available events and the cross sections provided by WHIZARD. Each event and its number represents its own integrated luminosity content L which can be calculated via

$$L = \frac{N}{\sigma}.$$

Therefore the corresponding luminosity of each sample is also listed in the tables.

As expected, the cross sections for all processes for one electric charge of the top quark agree within the statistical errors.

process	number of events	cross section [fb]	luminosity [fb^{-1}]
pp→b$\bar{\text{b}}$ud$\bar{\text{e}}^-\bar{\nu}_e\gamma$	25000	197.52±0.44	126.57±0.28
pp→b$\bar{\text{b}}$c$\bar{\text{s}}$e$^-\bar{\nu}_e\gamma$	25000	198.84±0.52	125.73±0.32
pp→b$\bar{\text{b}}$d$\bar{\text{u}}$e$^+\nu_e\gamma$	25000	198.98±0.34	125.64±0.21
pp→b$\bar{\text{b}}$s$\bar{\text{c}}$e$^+\nu_e\gamma$	25000	199.41±0.42	125.37±0.26

Table 5.1: Generated 7-particle final state samples with an electric charge of $Q_t = \frac{2}{3}$ for the top quark.

process	number of events	cross section [fb]	luminosity [fb^{-1}]
pp→b$\bar{\text{b}}$ud$\bar{\text{e}}^-\bar{\nu}_e\gamma$	25000	255.72±0.95	97.76±0.36
pp→b$\bar{\text{b}}$c$\bar{\text{s}}$e$^-\bar{\nu}_e\gamma$	25000	252.64±0.77	98.96±0.30
pp→b$\bar{\text{b}}$d$\bar{\text{u}}$e$^+\nu_e\gamma$	25000	257.27±0.79	97.17±0.30
pp→b$\bar{\text{b}}$s$\bar{\text{c}}$e$^+\nu_e\gamma$	25000	255.55±0.79	97.83±0.30

Table 5.2: Generated 7-particle final state samples with an electric charge of $Q_t = -\frac{4}{3}$ for the top quark.

5.3 Event Selection

On detector level, top quark events can only be determined by their final state particles. Therefore, algorithms and cuts have to be applied and optimized to identify the signature of certain physics objects with a high efficiency and purity. The 7-particle final state events in this analysis requires excellent identification and measurement of electrons, jets, which are induced by the two bottom quarks and the two light quarks in each event, photons and missing transverse energy, as neutrinos cannot be measured directly.

In each event, the top quark pair candidates are choosen with standard selection cuts recommended by the ATLAS Top Cross Section group [54]. In a addition, selection cuts on the photons have been performed, which are comform with the guidelines of the ATLAS top group for the CSC notes [55].

The following analysis has also been done with the ATLAS framework ATHENA (version 15.3.0). Primarily, packages are used which are provided by th ATLAS top reconsruction group, in particular the algorithm TopCommissioning [56].

5.3.1   Trigger

The function of the trigger and its different levels has been described in section 2.6. In this analysis, an event passes the trigger if the single isolated electron trigger e15_medium has fired. This trigger involves a transverse momentum threshold of 15 GeV, as well as only electrons identified as "medium" (see next subsection).

5.3.2   Electrons

Electron candidates are reconstructed by informations of the calorimeters and inner tracker of ATLAS. The likelihood analysis IsEM is used for electron identification. Each electron candidate has to pass a series of cuts based on the shower shape properties in different compartments of the calorimeter, variables combining ID and Calo informations as well as cuts on tracking information. By the number and types of passed cuts, the electrons are defined as "loose", "medium" and "tight". "Medium" electrons are used in this analysis. Furthermore, these leptons are required to have pseudorapidity in the range $0 \leq |\eta| \leq 2.47$ and $p_T > 20$ GeV. If a candidate is found in the calorimeter crack region, $1.37 \leq |\eta| \leq 1.52$, the candidate is discarded. Finally, accepted electrons are required to be isolated based on calorimeter energy. The additional transverse energy E_T in a cone with radius $\Delta R = 0.2$ around the electron axis is required to be less than 6 GeV. Only those events are used in this analysis, where exactly one electron agrees to all conditions.

5.3.3   Jets

Jets are reconstructed with the standard ATLAS cone algorithm in $\eta - \varphi$ space, with a cone radius of 0.4, based on energy deposits in calorimeter towers of size $\Delta\eta \times \Delta\varphi = 0.1 \times 0.1$. In each event, at least four jets are required to have a minimum transverse momentum of $p_T > 20$ GeV, of which at least three have $p_T > 40$ GeV, all with a pseudorapidity of $|\eta| \leq 2.5$. Jets are removed if they overlap with a good electron within a cone of size $\Delta R = 0.4$.

5.3.4   Missing Transverse Energy

Various contributions are taken into account for the missing transverse energy E_T (MET): The cells in an identified electron or photon cluster, inside jets, or in topological clusters outside identified objects. An event passes the selection, if $E_T > 20$ GeV.

5.3.5   Photons

The selection of photons is similar to the one for electrons. Photon candidates are also identified by the method IsEM, which differs in the variety of cuts compared to the

electrons due to the lack of photon track information. Photons pass the selection, if they are identified as "tight". In addition, the candidates are required to have a transverse momentum above $10\,\text{GeV}$ and pseudorapidity in the range $0 \leq |\eta| \leq 2.47$, except for the calorimeter crack region $1.37 \leq |\eta| \leq 1.52$.

5.3.6 Selection Results

The baseline cuts are applied in a defined sequence:

1. Electron Trigger including electron identification

2. Exactly one "good" electron

3. Transverse missing energy above $20\,\text{GeV}$

4. At least three jets with $p_T > 40\,\text{GeV}$

5. At least four jets with $p_T > 20\,\text{GeV}$

6. At least one "good" photon with $p_T > 10\,\text{GeV}$

This selection has been performed separately for both possible electric charges of the top quark, with the results shown in Tables 5.3 and 5.4. Besides the total number of events which have remained after each cut, the efficiency after each cut and the cumulative efficiency are listed.

cut	number of events	cut efficiency [%]	total efficiency [%]
1	14,667	14.67	14.67
2	12,276	83.70	12.28
3	10,841	88.31	10.84
4	6,119	56.44	6.12
5	5,137	83.95	5.14
6	2,073	40.35	2.07

Table 5.3: Selection results after each cut for 100,000 Standard Model events. Each of the cut efficiencies has an error smaller 0.70%, while the total efficiency errors are smaller than 0.11%.

The results show a total efficieny of 2.07% for the Standard Model and 2.82% for the exotic model. The acceptance of the selection of top quark events (without photon selection) is very low compared to the latest results of the ATLAS top cross section group. The analysis group has stated in [57] a selection efficiency of 18.9% for electron events. But as they have used samples which include semileptonic events with electrons and muons as well as fully leptonic events with both lepton types, the resulting efficiency in this thesis should be even higher. For further investigation, the official ATLAS sample with ID 105205 has been used for comparison. The $t\bar{t}$ process in this sample has been simulated

cut	number of events	cut efficiency [%]	total efficiency [%]
1	15,766	15.77	15.77
2	13,330	84.55	13.33
3	11,474	86.08	11.47
4	7,256	63.24	7.26
5	6,343	87.42	6.34
6	2,815	44.38	2.82

Table 5.4: Selection results after each cut for 100,000 events of the exotic top quark model. Each of the cut efficiencies has an error smaller 0.63%, while the total efficiency errors are smaller than 0.12%.

with AcerMC interfaced to Pythia for the parton showers. The selection cuts (without photon selection) have been applied to 10,000 events after being identified as semileptonic electron events, with the results shown in Table 5.5.

The comparison of the cut efficiencies in Table 5.5 with the cut efficiencies in Tables 5.3 and 5.4 show a big discrepancy in the result for the first cut. The reason has been found in the algorithm IsEM. After the comparison of each variable included in the "medium" electron search, the single variable TrackA0 has shown a big difference between the official ATLAS sample and the samples generated for this thesis. TrackA0 is the so-called transverse impact parameter which describes the distance at the point of closest approach between the beam or z-axis and the extrapolation of a reconstructed electron track in the transverse plane (r-ϕ). This distance has to be smaller than 1 mm, otherwise the electron is dropped. The variable TrackA0 showed an efficiency of 85.5% for the official sample and 27.4% for the sample produced for this thesis. Reasons for this discrepancy are unknown so far and are being investigated further.

The results provided in the next section use the efficiency from the samples produced for this thesis. The results are therefore conservative.

cut	number of events	cut efficiency [%]	total efficiency [%]
1	6,845	68.45	68.45
2	5,148	75.21	51.47
3	4,657	90.46	46.56
4	2,427	52.12	24.27
5	2,003	82.53	20.03

Table 5.5: Selection results after each cut for 10,000 semileptonic electron-events of official ATLAS sample 105205

5.4 Separation Between Electric Charge Models Of The Top Quark

Finally, a method is developed to distinguish between the electric charge predicted by the Standard Model and the exotic electric charge for the top quark. In the previous chapter, the invariant mass distributions of the top quark have shown distinctive shape differences between both top quark models (see Section 4.4.3). Especially, the invariant mass distribution, which include the photon in the reconstruction (Figure 4.16, right), offers an explicit possibility to define a discrimination variable. It shows two peaks, one at the top quark mass and another broader peak above the mass of the top quark. While the top quark mass peak is higher for the Standard model distribution, the second peak is more disctinctive for the exotic model. Dividing these distributions at the minimum value m_{cut} between the two peaks, a discrimination variable D can be defined by

$$D = \frac{\text{Number of events with an invariant mass } m_{inv} \leq m_{cut}}{\text{Number of events with an invariant mass } m_{inv} > m_{cut}}.$$

As this is essentially a ratio of cross sections, the value of the discrimination variable is independent of the integrated luminosity (see Section 5.2). Therefore, the same ratio D is expected for any integrated luminosity.

Only statistical errors are considered in this analysis. Hence, the errors are calculated as:

- Number of events M with $m_{inv} \leq m_{cut}$: $\sigma(M) = \sqrt{M}$

- Number of events N with $m_{inv} > m_{cut}$: $\sigma(N) = \sqrt{N}$

- Discrimination variable $D = \frac{M}{N}$: $\sigma(D) = \sqrt{\frac{1}{N^2}\sigma^2(M) + \frac{M^2}{N^4}\sigma^2(N)} = \sqrt{\frac{M}{N^2} + \frac{M^2}{N^3}}$

The error of the ratio D depends on the total number of events and will become smaller with higher integrated luminosity.

The expected value of the discrimination variable D is calculated for both top quark models. All datasets are used for calculation to get results with highest accuracy and smallest errors as possible. This results in an exptected ratio D_{exp}^{SM} for the Standard Model and D_{exp}^{XM} for the exotic model.

Then, the observed value is determined for a fixed integrated luminosity. As no real data is available up to now, it is assumed in this analysis that the measurements with the ATLAS detector will confirm the top quark electric charge predicted by the Standard Model. Hence, the observed ratio is determined with the samples including the Standard Model, resulting in a ratio D_{obs}. A number of events N' for given integrated luminosity L' can be calculated by

$$N' = \frac{N}{L} \cdot \epsilon \cdot L'$$

N is the number of events at a luminosity L and ϵ the selection efficiency determined in the last section. In this case, L is the integrated luminosity of all four Standard Model data samples, $L = (125.83 \pm 0.27)\,\text{fb}^{-1}$, and ϵ the Standard Model selection efficiency, $\epsilon = 2.08\%$.

Finally, the exotic top quark model can be excluded with the significance S, which can be determined by:

$$S = \frac{\text{expected value for exotic model - observed value}}{\text{error of observed value}} = \frac{D_{\text{exp}}^{\text{XM}} - D_{\text{obs}}}{\sigma(D_{\text{obs}})}$$

5.4.1 Separation On Parton Level

In order to establish the described separation method, it is first applied on parton level. For the calculation of the expected value, all data samples are used, which have been also used for the invariant mass distributions in Figure 4.16 and for the full simulation production. As the invariant mass has been determined for the hadronic top quark and the leptonic top quark, each distribution consists of 200,000 events. The minimum between the peaks is around 178 GeV for both distributions, which is hence defined as m_{cut}. The distributions are shown again in Figure 5.2 with m_{cut} marked by a vertical line. The number of events below and above 178 GeV as well as the resulting ratio D are listed in Table 5.6.

The observed value of D is calculated for an integrated luminosity of $1\,\text{fb}^{-1}$. For the Standard Model, a total of 33 events are expected, with 12 events of an invariant mass below 178 GeV and 21 events above m_{cut}. This results in an observed ratio of

$$D_{\text{obs}} = 0.57 \pm 0.21$$

Therefore, the exotic model can be excluded at an integrated luminosity of $1\,\text{fb}^{-1}$ with a significance S of

$$S = 1.48\,\sigma$$

A $5\,\sigma$ exclusion can be achieved at an integrated luminosity of

$$L = 12.70\,\text{fb}^{-1}$$

with 148 events of an invariant mass below m_{cut} and 272 events with an invariant mass above m_{cut}.

	Events with $m_{\text{inv}} \leq m_{\text{cut}}$	Events with $m_{\text{inv}} > m_{\text{cut}}$	D_{exp}	$\sigma(D_{\text{exp}})$
Standard Model	70343	129657	0.543	0.003
Exotic model	41857	158143	0.265	0.001

Table 5.6: A total of 200,000 events are used for both top quark models to determine the expected ratio D_{exp}. The number of events below and above m_{cut} are listed, as well as the resulting ratio D_{exp} and its error $\sigma(D_{\text{exp}})$.
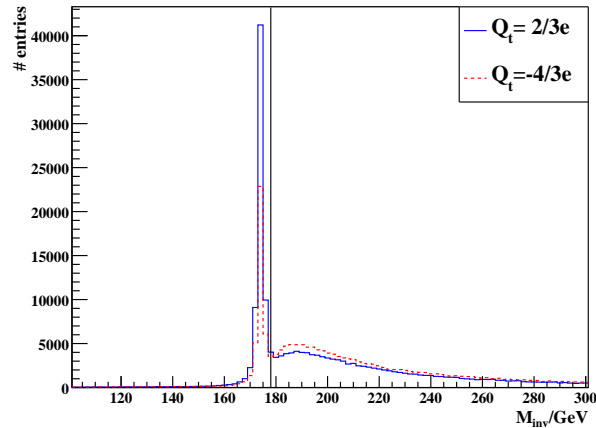
Figure 5.2: Invariant mass distributions of the Standard Model top quark (solid line) and the exotic top quark (dashed line) on parton level.The photon is included in the calculation of the invariant mass. The vertical line at a value of 178 GeV represents the cut, which is used to divide both distributions.

5.4.2 Separation On Detector Level

First, the invariant mass distributions have to be constructed on detector level.
It is impossible to assign the decay products of the top and antitop quark unambiguously on detector level, hence an established method is employed [57]:

- The hadronically decayed top quark is reconstructed with the three jets whose total transverse momentum, i.e. the p_T of the sum of the three energy-momentum vectors, is the highest amongst all three jet combinations.

- The leptonic branch is reconstructed with the highest remaining p_T jet after the jets for the hadronic top have been selected. The top quark is completed with the electron and the missing transverse momentum.

First, the distributions are calculated and compared with the histograms on parton level (Figure 4.15). The histograms in Figure 5.3 show the invariant mass distributions of the hadronic and leptonic top quark for both top quark models. The calculation has been performed with all events which have passed the event selection. In order to compare the shapes like on parton level, all distributions have been normalized to 1, i.e. the sum of all entries of a distribution is 1.
Huge effects of the detector response and the mass reconstruction method are visible in the distributions which include the photon in the calculations. The two peaks at the top quark mass and at higher mass have merged and cannot be separated. Furthermore, the spectra of both top models are similar but still the distributions for the exotic top quark are shifted towards larger masses.
For the calculation of the expected ratios D_{exp}^{SM} and D_{exp}^{XM}, all events are used, which have passed the event selection. In order to maximize the statistics, the hadronic and leptonic top quarks are combined in one distribution, resulting in 4,146 events for the Standard Model and 5,630 events for the exotic model. As no cut value m_{cut} can be determined, it

is set at the parton level value of 178 GeV (Figure 5.4). The number of events below and above 178 GeV as well as the resulting ratios are listed in Table 5.7.

	Events with $m_{inv} \leq m_{cut}$	Events with $m_{inv} > m_{cut}$	D_{exp}	$\sigma(D_{exp})$
Standard Model	897	3249	0.276	0.010
Exotic model	837	4793	0.175	0.007

Table 5.7: All events, which have passed the event selection, are used to determine the expected ratio D_{exp} for both top quark models. The number of events below and above m_{cut} are listed, as well as the resulting ratio D_{exp} and its error $\sigma(D_{exp})$.

The observed value D_{obs} is also calculated for an integrated luminosity of $1\,fb^{-1}$. For the Standard Model, 7 events are expected with an invariant mass below 178 GeV and 26 events with an invariant mass above m_{cut}. This results in an observed ratio of

$$D_{obs} = 0.33 \pm 0.27$$

Therefore, the exotic model can be excluded at an integrated luminosity of $1\,fb^{-1}$ with a significance S of

$$S = 0.77\,\sigma$$

A $5\,\sigma$ exclusion can be achieved at an integrated luminosity of

$$L = 37.95\,fb^{-1}$$

with 271 events of an invariant mass below m_{cut} and 980 events with an invariant mass above m_{cut}.

The expected ratios D_{exp}^{SM} and D_{exp}^{XM} are much smaller than the expected values on parton level. While the ratio D_{exp}^{SM} of the Standard Model is two times higher, D_{exp}^{XM} of the exotic model is 1.5 times higher on parton level. Furthermore, the difference between both expected values is reduced compared to the parton level result from 0.278 to 0.101. These factors have effected the observed value D_{obs} as well as the the Significance S, which is two times smaller than in the four vectors calculations.
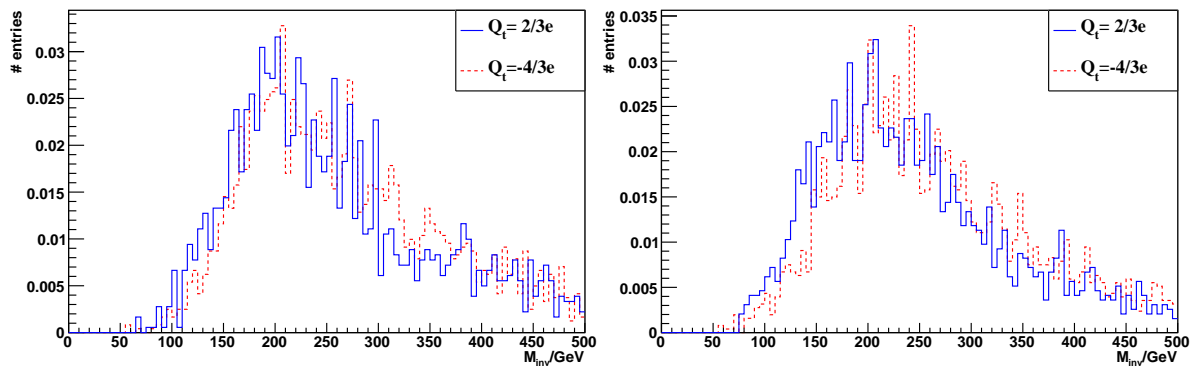
Figure 5.3: Invariant mass distributions of the Standard Model top quark (solid line) and the exotic top quark (dashed line) on detector level. The hadronic top quark distributions are shown on the left and the leptonic top quark distributions on the right.
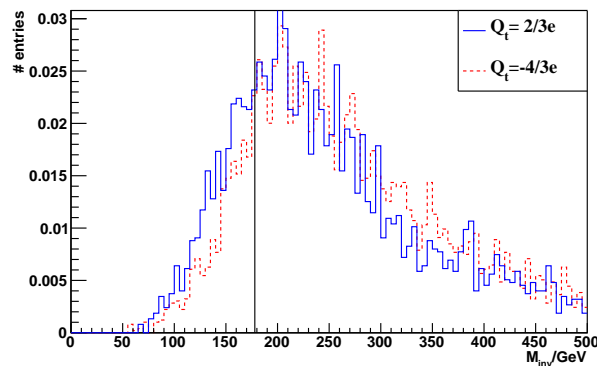
Figure 5.4: Invariant mass distributions of the Standard Model top quark (solid line) and the exotic top quark (dashed line) on detector level. The vertical line at a value of $178\,\mathrm{GeV}$ represents the cut, which is used to divide both distributions.

5.5 Summary

This chapter has presented a method to distinguish between the two possible top quark electric charges. A discrimination variable is defined, which relies on the shape of the invariant mass distribution of the top quark rather than on the absolute cross section. Using the electron channel of the radiative top quark processes, a $5\,\sigma$ exclusion can be achieved at an integrated luminosity of $37.95\,\mathrm{fb}^{-1}$.

In order to establish this method, it has been applied first on parton level. For an integrated luminosity of $1\,\mathrm{fb}^{-1}$, the exotic model can be excluded with a significance of $1.48\,\sigma$. On parton level the features of the radiative top decay are clearly visible. It is therefore well suited to establish the procedure to distinguish between the two top quark models.

On detector level, the distributions do not show the distinctive features of the parton level distributions. Reasons for this are the included detector response, as well as the ambiguous method to reconstruct the invariant mass. The discrimination method has still been applied, but high deviations can be observed in the detector level results compared

to the exact results on parton level. For the same integrated luminosity of $1\,\mathrm{fb}^{-1}$, the exotic model can be excluded on detector level with a significance of $0.77\,\sigma$, while a $5\,\sigma$ exclusion can be achieved at an integrated luminosity of $37.95\,\mathrm{fb}^{-1}$. In order to optimize the invariant mass reconstruction, other methods have to studied.

The selection of top quark events has shown an efficiency of 2.07% for the Standard Model and 2.82% for the exotic model. A comparison with an official ATLAS data sample has indicated that the expected selection efficiency should be three to four times higher. Hence, the number of events at an integrated luminosity of $1\,\mathrm{fb}^{-1}$ should rise by the same factor as the selection efficiency, resulting in a higher exclusion significance than the calculated value.

No background processes have been considered in this chapter and still have to be included.

Chapter 6

Summary And Outlook

The aim of this thesis has been the electric charge determination of the top quark. In Section 4.1 it has been shown that only two values are possible, $\frac{2}{3}$e, which is predicted by the Standard Model, and an exotic electric charge of $-\frac{4}{3}$e. Therefore, the electric charge of the top quark is determined in this thesis by developing a method to distinguish between both possible values.

One proposed technique is the direct measurement of the top quark electromagnetic coupling through photon radiation. It has been described in Section 4.2.1 that the cross sections of photon radiative top quark processes show a dependence on the electric charge of the top quark Q_t, since the coupling of photons to the top quark is directly proportional to $|Q_t^2|$. Hence, it is expected that cross sections calculations would show different results for the two possible electric charges.

This technique has been investigated further by calculating the phase space of radiative top quark processes for both top quark models. The calculations have been performed for different final states, with the resulting cross sections presented in Section 4.4.1. The results have confirmed the electric charge dependence with noticable higher cross sections of the exotic model compared to the Standard Model for all calculated 3-, 5- and 7-particle final states.

As the measurement of the absolute cross section will have large uncertainties in the beginning of the data taking with the ATLAS detector, a method relying on the the shape of the variables rather than the total number of events is investigated. Various kinematic distributions have been reconstructed for both top quark models and compared. The best discrimination possibility is presented in the invariant mass distribution of the top quark, which include the photon in the invariant mass calculation (Section 4.4.2). The distribution features two peaks, one peak at the top quark mass, which is more pronounced for the Standard Model, and a second broader peak above the top quark mass, which is more distinctive for the exotic model.

These unique properties are used to develop a discrimination variable in order to distinguish between both possible top quark electric charges (Section 5.4). First, the distributions are divided at the minimum value m_{cut} between the two peaks. The discrimination variable is then defined as the ratio of the number of events with an invariant mass below m_{cut} and the number of events with an invariant mass above m_{cut}. This ratio does not depend on the integrated luminosity, and therefore the expected value is equal for any data

size, but its accuracy rises with higher statistics. The discrimination method has been applied on parton and on detector level, assuming that the measurements at the LHC with the ATLAS detector will confirm that the top quark has the electric charge predicted by the Standard Model. For an integrated luminosity of $1\,\mathrm{fb}^{-1}$, the exotic model can excluded on parton level with a significance of $1.48\,\sigma$ and on detector level with a significance of $0.77\,\sigma$. A $5\,\sigma$ exclusion can be achieved at an integrated luminosity of $12.70\,\mathrm{fb}^{-1}$ on parton level and $37.95\,\mathrm{fb}^{-1}$ on detector level.

Outlook

A discrimination method has been successfully developed in this thesis, but several aspects have still to be considered.

The problem regarding the very low selection efficiency around 2% has to be solved. It has to be investigated, why the parameter TrackA0 in the algorithm IsEM has an around three times smaller efficiency for the samples, which have been produced for this thesis, compared to official ATLAS data samples. The selection efficiency is expected to be three to four times higher than the calculated value of 2%.

This analysis has focused on the electron channel of the radiative top quark processes. Therefore, the muon channel ($\mathrm{pp}\rightarrow\mathrm{b\bar{b}q_1\bar{q}_2}\mu^{\pm}\nu_{\mu}\gamma$) has still to be included.

Furthermore, only statistical errors have been regarded. Hence, systematic errors have to be included, which occur for example due to uncertainties of the used parton density functions, the jet energy scale and the luminosity.

Finally, background processes have still to be considered. The dominant expected background for top quark processes are W+Jets events, but also $\mathrm{Wb\bar{b}}$, Z+Jets and single top events. The most relevant background for the photons is expected to be the $\pi^0 \rightarrow \gamma\gamma$ process.

Other methods like kinematic fitting should be tested for the reconstruction of the invariant mass distributions in order to improve its efficiency and purity.

Bibliography

[1] F. Abe et al. Observation of top quark production in pp collisions, 1995. hep-ex/9503002.

[2] S. Abachi et al. Observation of the top quark, 1995. hep-ex/9503003.

[3] S. W. Herb et al. Observation of a dimuon resonance at 9.5-GeV in 400-GeV proton-nucleus collisions, 1977.

[4] Tevatron Electroweak Working Group. Combination of CDF and D0 Results on the Mass of the Top Quark. 2009. arXiv:0903.2503v1.

[5] D. Griffiths. *Introduction to Elementary Particles*. John Wiley & Sons, 1987.

[6] F. Halzen and A. D. Martin. *Quarks and Leptons: An Introductory Course in Modern Particle Physics*. John Wiley & Sons, 1984.

[7] Standard Model. http://en.wikipedia.org/wiki/Standard_Model.

[8] P. W. Higgs. Broken symmetries, massless particles and gauge fields. *Phys. Lett.*, 12:132–133, 1964.

[9] C. Amsler et al. (Particle Data Group). The Review of Particle Physics, 2008.

[10] M. E. Peskin and D. R. Schroeder. *An Introduction to Quantum Field Theory*. Westview Presss, 1995.

[11] O. Biebel. Experimental tests of the strong interaction and its energy dependence in electron positron annihilation. *Phys. Rept.*, 340:165–289, 2001.

[12] J. Pumplin et al. New generation of parton distributions with uncertainties from global QCD analysis, 2002. hep-ph/0201195.

[13] ATLAS cross sections used with the 10TeV production. https://twiki.cern.ch/twiki/bin/view/AtlasProtected/TopReferences10TeV.

[14] Useful Diagrams of Top Signals and Backgrounds. http://www-d0.fnal.gov/Run2Physics/top/top_public_web_pages/top_feynman_diagrams.html.

[15] J. R. Ellis and G. L. Fogli. The mass of the top quark from electroweak radiative corrections. *Phys. Lett.*, B213, 1988.

[16] ATLAS collaboration. Expected performance of the ATLAS experiment : detector, trigger and physics, 2008. CERN-OPEN-2008-020, arXiv:hep-ph/0901.0512v3.

[17] CERN. Incident in LHC sector 3-4. Press Release PR09.08, http://press.web.cern.ch/press/PressReleases/ Releases2008/PR09.08E.html.

[18] CERN. The LHC is back. Press Release PR16.09, http://press.web.cern.ch/press/PressReleases/ Releases2009/PR16.09E.html.

[19] CERN. Two circulating beams bring first collisions in the LHC. Press Release PR17.09, http://press.web.cern.ch/press/PressReleases/ Releases2009/PR17.09E.html.

[20] CERN. LHC to run at 3.5TeV for early part of 2009-2010 run rising later. Press Release PR13.09, http://press.web.cern.ch/press/PressReleases/ Releases2009/PR13.09E.html.

[21] O. S. Bruening et al. LHC Design Report, Vol. 1: The LHC Main Ring. 2004. CERN-2004-003-V-1, http://cdsweb.cern.ch/record/782076.

[22] M. Benedikt et al. LHC Design Report, Vol. 3: The LHC Injector Chain. 2004. CERN-2004-003-V-3, http://cdsweb.cern.ch/record/823808.

[23] L. Foa A. Herve M. Della Negra and A. Petrilli. CMS Physics Technical Design Report. 2006. CERN-LHCC-2006-001, http://cdsweb.cern.ch/record/922757.

[24] LHCb collaboration. LHCb Technical Proposal. 1998. CERN-LHCC-98-004.

[25] L. Riccati K. Safarik C.W. Fabjan and H. de Groot. ALICE Physics Performance Technical Design Report. 2005. CERN-LHCC-2005-030, http://cdsweb.cern.ch/record/879894.

[26] CERN FAQ – LHC the guide, 2006.

[27] The four main LHC experiments. CERN-AC-9906026, http://cdsweb.cern.ch/record/40525.

[28] ATLAS collaboration. The ATLAS Experiment at the CERN Large Hadron Collider. 2008. JINST 3 S08003.

[29] ATLAS Collaboration. ATLAS Magnet System: Technical Design Report. 1997. CERN-LHCC-97-018, http://cdsweb.cern.ch/record/338080.

[30] ATLAS collaboration. ATLAS Inner Detector: Technical Design Report Vol.1. 1997. CERN-LHCC-97-016, http://cdsweb.cern.ch/record/331063.

[31] ATLAS collaboration. ATLAS Inner Detector: Technical Design Report Vol.2. 1997. CERN-LHCC-97-017.

[32] ATLAS Collaboration. ATLAS Pixel Petector: Technical Design Report. 1998. CERN-LHCC-98-013.

[33] A. Ahmad et al. The Silicon Microstrip Sensors of the ATLAS Semiconductor Tracker. *Nucl. Instrum. Methods Phys. Res.*, A 578, 2007.

[34] E. Abat et al. The ATLAS Transition Radiation Tracker (TRT) Proportional Drift Tube: Design and Performance. 2008. J. Instrum. 3 (2008), P02013.

[35] ATLAS Collaboration. ATLAS Calorimeter Performance: Technical Design Report. 1996. CERN-LHCC-96-040.

[36] ATLAS Collaboration. ATLAS Calorimeter Performance: Technical Design Report. 1996. CERN-LHCC-96-041.

[37] ATLAS Collaboration. ATLAS Calorimeter Performance: Technical Design Report. 1996. CERN-LHCC-96-042.

[38] ATLAS Collaboration. ATLAS Muon Spectrometer: Technical Design Report. 1997. CERN-LHCC-97-022.

[39] ATLAS Collaboration. ATLAS Level 1 Trigger: Technical Design Report. 1998. CERN-LHCC-98-014, http://cdsweb.cern.ch/record/381429.

[40] ATLAS Collaboration. ATLAS High Level Trigger, Data Acquisition and Controls: Technical Design Report. 2003. CERN-LHCC-2003-022, http://cdsweb.cern.ch/record/616089.

[41] ATLAS Collaboration. ATLAS Trigger Performance: Status Report. 1998. CERN-LHCC-98-015, http://cdsweb.cern.ch/record/381430.

[42] D0 Collaboration. Experimental Discrimination between Charge 2e/3 Top Quark and Charge 4e/3 Exotic Quark Production Scenarios. *Phys. Rev. Lett.*, PRL 98, 041801, 2007.

[43] CDF Collaboration. First CDF Measurement of the Top Quark Charge using the Top Decay Products. 2007. CDF note 8967.

[44] We-Fu Chang Darwin Chang and Ernest Ma. Alternative Interpretation of the Tevatron Top Events. *Phys. Rev.*, D59, 091503, 1999.

[45] M. Jurcovicova S. Tokar M. Ciliak and U. Baur. Top charge measurement at ATLAS detector. 2003. ATLAS Note PHYS-2003-35.

[46] W. Kilian, T. Ohl, and J. Reuter. WHIZARD: Simulating Multi-Particle Processes at LHC and ILC. 2007. arXiv:0708.4233.

[47] W. Kilian, T. Ohl, and J. Reuter. WHIZARD 1.93: A generic Monte-Carlo integration and event generation package for multi-particle processes. 2001. LC-TOOL-2001-039.

[48] S. Mrenna T. Sjostrand and P. Skands. PYTHIA 6.4 physics and manual, 2006. hep-ph/0603175.

[49] G. Corcella et al. Herwig 6.5. 2001. hep-ph/0210213.

[50] M. Moretti, T. Ohl, and J. Reuter. O'Mega: An Optimizing Matrix Element Generator. 2001. hep-ph/0102195.

[51] R. C. Group D. Bourilkov and M. R. Whalleyâ . LHAPDF: PDF Use from the Tevatron to the LHC. 2006. arXiv:hep-ph/0605240v2.

[52] LHC Experiments Committee. ATLAS computing: Technical Design Report, 2005. CERN-LHCC-2005-022, http://cdsweb.cern.ch/record/837738.

[53] Parameters for ATLAS MC production 2008. https://twiki.cern.ch/twiki/bin/view/AtlasProtected/McProductionCommonParameters08.

[54] ATLAS collaboration. Prospects for the Top Pair Production Cross-section at $\sqrt{s}$= 10 TeV in the Single Lepton Channel in ATLAS , 2009. ATL-PHYS-PUB-2009-087, http://cdsweb.cern.ch/record/1200436.

[55] ATLAS top group guidelines for CSC notes. https://twiki.cern.ch/twiki/bin/view/AtlasProtected/TopGroupCSCObjectSelection.

[56] ATLAS top reconstruction group. https://twiki.cern.ch/twiki/bin/view/AtlasProtected/TopReconstructionGroup.

[57] ATLAS collaboration. Prospects for measuring the Top Quark Pair Production Cross-section in the Single Lepton Channel at ATLAS in 10 TeV pp Collisions , 2009. Preliminary draft, https://twiki.cern.ch/twiki/bin/view/ AtlasProtected/TopSingleleptonPubNote.

Erklärung

Hiermit erkläre ich, dass ich die vorliegende Masterarbeit selbständig verfasst und keine anderen als die angegebenen Quellen und Hilfsmittel benutzt sowie Zitate und Ergebnisse Anderer kenntlich gemacht habe.

_____   _____

(Ort, Datum)   (Unterschrift)